Influence of SnBi Antisite Defects on the Electronic Band Structure and Transport Properties of the Layered Chalcogenide Semiconductor SnBi2Te4

Ilayda Terzi, Kacper Pryga, Bartlomiej Wiendlocha, Petr Levinský, Soufiane El Oualid, Sylvie Migot, Jaafar Ghanbaja, Christine Gendarme, Thierry Schweitzer, Bernard Malaman, et al.

To cite this version:

Ilayda Terzi, Kacper Pryga, Bartlomiej Wiendlocha, Petr Levinský, Soufiane El Oualid, et al.. Influence of SnBi Antisite Defects on the Electronic Band Structure and Transport Properties of the Layered Chalcogenide Semiconductor SnBi2Te4. Journal of Physical Chemistry C, 2024, 10.1021/acs.jpcc.4c06097 . hal-04755330

HAL Id: hal-04755330
https://hal.science/hal-04755330v1

Submitted on 27 Oct 2024

Influence of Sn_{Bi} Antisite Defects on the Electronic Band Structure and Transport Properties of the Layered Chalcogenide Semiconductor $SnBi_2Te_4$

Ilayda Terzi,[1] Kacper Pryga,[2] Bartlomiej Wiendlocha,[2,*] Petr Levinský,[3] Soufiane El Oualid[1], Sylvie Migot[1], Jaafar Ghanbaja[1], Christine Gendarme[1], Thierry Schweitzer[1], Bernard Malaman,[1] Gérard Le Caër,[4] Bertrand Lenoir,[1] Christophe Candolfi[1,*]

[1] *Institut Jean Lamour, UMR 7198 CNRS – Université de Lorraine, 2 allée André Guinier-Campus ARTEM, BP 50840, 54011 Nancy Cedex, France*

[2] *AGH University of Krakow, Faculty of Physics and Applied Computer Science, Aleja Mickiewicza 30, 30-059 Krakow, Poland*

[3] *FZU – Institute of Physics of the Czech Academy of Sciences, Cukrovarnická 10/112, 16200, Prague 6, Czech Republic*

[4] *Institut de Physique de Rennes, UMR UR1-CNRS 6251, Université de Rennes I, Campus de Beaulieu, 35042 Rennes Cedex, France*

ABSTRACT

Narrow-band-gap, layered chalcogenide semiconductors provide a rich area of research for designing highly-efficient thermoelectric materials for near-room-temperature applications due to their intrinsically low lattice thermal conductivity and multivalley electronic band structure. Here, we report on a comprehensive theoretical and experimental investigation of the thermoelectric properties of one member of this class, $SnBi_2Te_4$, in the temperature range of 5–700 K. Polycrystalline samples crystallize with a rhombohedral crystal structure described in the $R\bar{3}m$ space group (No. 166) with room-temperature lattice parameters a = 4.398(1) Å and

$c = 41.615(1)$ Å. To probe the electronic tunability of $SnBi_2Te_4$, the synthesis of an Sn-deficient sample $Sn_{0.95}Bi_2Te_4$ was attempted but led to an intergrowth of $SnBi_2Te_4$ and $SnBi_4Te_7$, indicating that only a very limited range of Sn-deficiency can exist. Transport properties measurements combined with electronic band structure calculations show that $SnBi_2Te_4$ is a p-type, narrow-band-gap semiconductor with a multivalley valence band structure and a strong asymmetry between the valence and conduction bands. The presence of Sn_{Bi} antisite defects, supported by Mössbauer spectroscopy, plays an important role in shaping the electronic transport properties through a decrease in the electronic band gap and a reduction in the hole mobility, which causes the onset of bipolar conduction near 350 K. Some degree of anisotropy in the electrical resistivity and thermal conductivity measured parallel and perpendicular to the pressing direction exists, while the thermopower remains nearly isotropic. The complex crystal structure of $SnBi_2Te_4$ contributes to the very low lattice thermal conductivity of the order of 0.5 W m^{-1} K^{-1} at 300 K, leading to peak ZT values of 0.32 at 350 and 400 K for $Sn_{0.95}Bi_2Te_4$ and $SnBi_2Te_4$, respectively.

1. INTRODUCTION

Thermoelectric materials enable conversion of a temperature difference into electrical power and vice-versa, providing an emission-free and versatile way to harvest low-grade heat or to cool electronic devices.[1,2] The thermoelectric performance of a material is quantitatively captured by the dimensionless thermoelectric figure of merit $ZT = \alpha^2 T/\rho(\kappa_{el} + \kappa_{lat})$ where T is the absolute temperature, α is the thermopower (or Seebeck coefficient), ρ is the electrical resistivity and κ_{el} and κ_{lat} are the electronic and lattice thermal conductivity, respectively.[1-3] Designing highly-efficient compounds, however, requires to meet a subtle balance between electronic and thermal properties, which are interdependent through the carrier concentration.

Common strategies to optimize the electronic properties (α, ρ and κ_{el}) rely on specific modifications of the electronic band structure such as resonant levels or band convergence.[4-8] Specific crystallographic characteristics such as loosely-bound atoms in oversized cages or tunnels, lone-pair-driven atomic off-centering or the formation of solid solutions are few examples of approaches that have been demonstrated to be effective in lowering κ_{lat} through either dynamic or static disorder.[9-13]

The design of thermoelectric materials for low and near-room-temperature cooling applications has received less attention than for medium-to-high temperatures, power generation applications. Good thermoelectric performance at low temperatures can be typically achieved in narrow-band-gap semiconductors and semimetals.[3,14] Bi_2Te_3-based alloys,[1,3,15-17] Mg_3Bi_2-based compounds,[18,19] $Bi_{1-x}Sb_x$ solid solutions[20] or $CsBi_4Te_6$ (Ref. 21) are the few known examples of compounds where high ZT values could be obtained at or below 300 K. To mitigate the deleterious effect of minority carriers, promising candidate materials should possess a high majority-to-minority carrier weighed mobility ratio, that is, a high asymmetry between the conduction and valence band parameters.[14,22] Searching for narrow-band-gap semiconductors with these desired properties may therefore uncover novel efficient thermoelectric materials able to operate near room temperature.

In addition to providing a rich diversity of electronic and magnetic phenomena that notably include magnetic topological states and superconductivity,[23-28] compounds belonging to the homologous series $(A^{IV}Te)_n(Bi_2X_3)_m$ (A^{IV} = Ge, Sn or Pb ; X = Se or Te ; n and m are integers) exhibit tuneable narrow band gaps, along with structural and compositional complexity that make them interesting candidates for thermoelectric applications.[29-31] They adopt a trigonal crystalline structure described in the $R\bar{3}m$ (No. 166, similar to the parent compounds Bi_2X_3) or $P\bar{3}m1$ (No. 164) space groups. The crystal structure consists of covalently-bonded quintuple and/or septuple layers that are stacked along the c axis following the sequence $\mathrm{Te_1}$-Bi-$\mathrm{Te_2}$-A^{IV}-$\mathrm{Te_2}$-Bi-$\mathrm{Te_1}$ (Figure 1). These blocks are either held together by Te–Te van der Waals interactions (for $n = m = 1$) or separated by quintuple interlayers characteristic of $\mathrm{Bi_2Te_3}$ (for $n > m$).

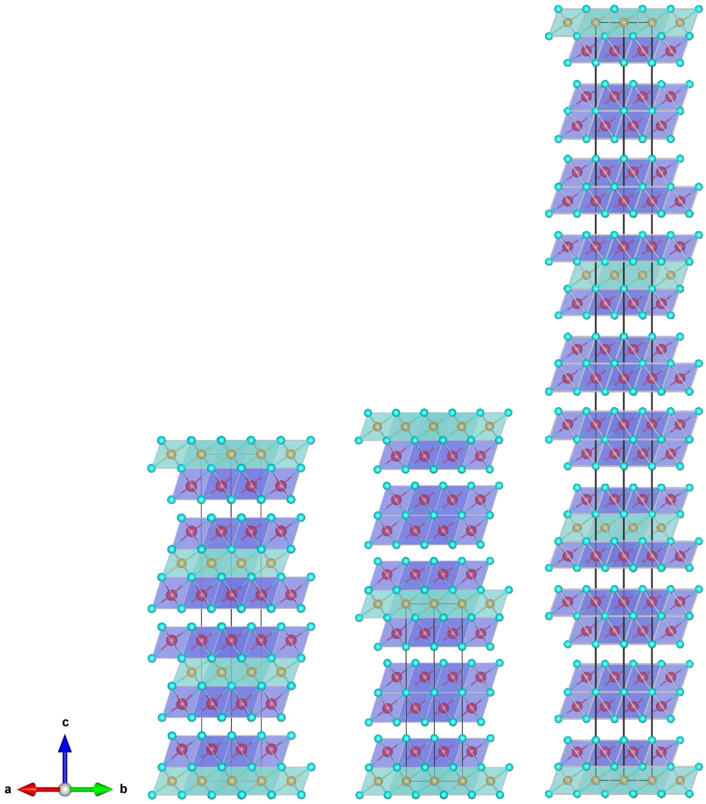

Figure 1. Crystal structures of $\mathrm{SnBi_2Te_4}$ (left), $\mathrm{SnBi_4Te_7}$ (middle) and $\mathrm{SnBi_6Te_{10}}$ (right). Both $\mathrm{SnBi_2Te_4}$ and $\mathrm{SnBi_6Te_{10}}$ crystallize in the $R\bar{3}m$ space group ($a = 4.935$ Å and $c = 41.606$ Å and $a = 4.930$ Å and $c = 102.470$ Å, respectively) while $\mathrm{SnBi_4Te_7}$ crystallizes in the $P\bar{3}m1$ space group ($a = 4.404$ Å and $c = 24.067$ Å). Sn, Bi and Te are represented by orange, red and light blue spheres. The environment of the Sn and Bi atoms is represented by the light and dark-blue octahedra. The structures are built up by the stacking of septuple layers ($\mathrm{SnBi_2Te_4}$) with one ($\mathrm{SnBi_4Te_7}$) and two ($\mathrm{SnBi_6Te_{10}}$) quintuple layers being added between two consecutive septuple layers.

Among this series, three line compounds were reported in the pseudo-binary phase diagram of the system $(\mathrm{SnTe})_n(\mathrm{Bi_2Te_3})_m$.[29,32] The more pronounced contrast in the atomic size between Sn-Te and Bi-Te layers is expected to yield very low lattice thermal conductivity values. Several experimental investigations have proposed that these compounds exhibit a certain degree of disorder within their crystal structure, primarily due to the mixed occupancy of Sn and Bi on the cationic sites.[33-35] Previous studies of their high temperature transport properties have shown that $SnBi_2Te_4$ and $SnBi_4Te_7$ are narrow-band-gap, degenerate *p*-type semiconductors.[36,37] Attempts to dope $SnBi_2Te_4$ by either acceptor or donor-like impurities have resulted in only small variations in the hole concentration,[37] suggesting that this compound is relatively impervious to conventional doping strategies.

While there have been several studies of $SnBi_2Te_4$ on either cold-pressed polycrystalline or single-crystalline specimens,[36,37] no detailed investigation on the low-temperature transport properties on dense polycrystalline samples has been reported so far. In addition, the degree of anisotropy in the transport properties measured parallel and perpendicular to the pressing direction has not been determined. In this work, we report on a comprehensive theoretical and experimental study of the transport properties of dense polycrystalline specimens of $SnBi_2Te_4$ over a broad range of temperatures (5 – 700 K). A further assessment of its electronic tunability was performed by synthesizing an Sn-deficient sample $Sn_{0.95}Bi_2Te_4$, with results indicating that only a very narrow range of deviations from the ideal stoichiometry exists for this phase. We notably demonstrate that the bipolar conduction that sets in near 350 K and strongly limits the thermoelectric performance in the mid-temperature range is a consequence of the presence of Sn_{Bi} antisite defects, which govern the electronic properties of $SnBi_2Te_4$.

2. EXPERIMENTAL AND COMPUTATIONAL METHODS

2.1. Synthesis. All of the elements and ingots were handled in a dry, Ar-filled glove box. Polycrystalline $SnBi_2Te_4$ and $Sn_{0.95}Bi_2Te_4$ samples were synthesized by direct reaction of high-purity elemental Sn (Alfa Aesar, 99.999%, purified), Bi (5N+, 99.999%, purified), Te (5N+, 99.999%, purified) in pre-evacuated, carbon-coated silica tubes sealed under inert atmosphere of Ar/H_2 mixture (95/5%). The sealed silica tubes were heated in a vertical furnace to 923 K, dwelt at this temperature for 4h before being quenched in room-temperature water. The obtained ingots were crushed and cold-pressed into several cylinders that were loaded into silica tubes, pumped to secondary vacuum and sealed under the same inert atmosphere for a subsequent annealing of 10 days at 823 K to improve the chemical homogeneity. An additional sample was annealed for 75 days at 823 K to assess the influence of long-term annealing on the structure at the atomic scale. The annealed polycrystalline ingots were crushed into fine powders that were loaded into a 10 mm diameter graphite die. These fine powders were consolidated by spark plasma sintering (SPS, Dr Sinter 515S, SPS syntex Inc.) at 673 K under a uniaxial pressure of 80 MPa for 5 min in vacuum. The cylindrical pellets obtained show a relative density higher than 95% of the theoretical density from crystallographic data. All subsequent chemical and physical characterizations have been performed on annealed, chemically-homogeneous samples. Except for powder X-ray diffraction, quenched samples were not further characterized.

2.2. Powder X-ray diffraction (PXRD). The crystal structure and phase purity of the samples were determined by powder X-ray diffraction at 300 K using a D8 Bruker Advance diffractometer equipped with a LynxEye detector (Cu $K\alpha_1$ radiation, $\lambda = 1.54056$ Å). The data were collected for 10h in the 2θ range of 10 – 150° with a step of 0.028°. Rietveld refinements of the unit cell parameters were performed with the FullProf suite.[38]

2.3. Scanning Electron Microscopy (SEM). SEM experiments were carried out on polished, dense pieces cut from the consolidated ingots using a Quanta FEG 650 (FEI). Backscattered electron (BSE) images and elemental X-ray mappings were collected to further assess the phase purity and the spatial distribution of the elements.

2.4. Electron Probe Microanalysis (EPMA). Bulk pieces of the consolidated samples were carefully polished using alumina powders below 1µm. The chemical composition of both samples was examined by EPMA using a JEOL JXA 8530F instrument equipped with wavelength-dispersive spectrometers. For $SnBi_2Te_4$, elemental Sn and Bi_2Te_3 were used as standards to determine the Sn, Bi, and Te concentrations, respectively. Owing to its nearly-stoichiometric composition, this sample was then used as a standard to determine the chemical composition of the $Sn_{0.95}Bi_2Te_4$ sample. The final chemical compositions were obtained by averaging the atomic percentages over more than 50 measurement spots for each sample.

2.5. Transmission Electron Microscopy (TEM). For these experiments, thin slices were prepared from pieces of the consolidated ingots by the dual focused ion beam (FIB, Helios NanoLab 600i, FEI) – scanning electron microscope system using the in-situ lift-out technique. High-resolution TEM (HRTEM), scanning TEM (STEM) in high-angle annular dark-field (HAADF) and annular bright-field (ABF) mode were performed with a JEOL ARM 200F – cold FEG TEM/STEM microscope operating at 200 keV, equipped with a spherical aberration (Cs) probe and image correctors.

2.6. Mössbauer spectroscopy. ^{119}Sn Mössbauer spectra were measured in transmission geometry with a spectrometer operating in the constant-acceleration mode. Spectra were recorded at 15 K in a JANIS (Research Company Inc.) liquid helium cryostat. Polycrystalline absorbers, with natural abundance of the ^{119}Sn isotope and an area density of ∼10 mg cm^{-2}, were used. The source, kept at room temperature, was $Ba^{119m}SnO_3$ with a nominal activity of 10 mCi. A 0.05 mm thick palladium foil was used as a critical absorber for Sn X-rays. The velocity calibration was performed against a 12-µm-thick α-Fe foil at 300 K using a source of ^{57}Co in Rh. ^{119}Sn isomer shifts (IS or δ) are referred with respect to $BaSnO_3$ at 300 K. Mössbauer spectra were fitted with a standard least-squares-method program assuming Lorentzian peaks.

2.7. Transport Properties Measurements. Due to the anisotropic crystal structure of $SnBi_2Te_4$, the transport properties were measured on samples cut perpendicular and parallel to the pressing direction. Electrical resistivity, thermopower and thermal conductivity were measured between 2 and 300 K using the thermal transport option of a physical property measurement system (PPMS, Quantum Design). Bar-shaped samples with typical dimensions 2.5×2.5×7 mm^3 were cut from the consolidated pellets with a diamond-wire saw. Four copper leads were attached onto the samples with a low-melting-point braze to achieve good electrical and thermal contacts. Hall effect was measured on the same samples using the AC transport option of the PPMS in a five-probe configuration. Five copper wires were brazed onto the samples. The transverse electrical resistivity ρ_{xy} was measured between 5 and 300 K under magnetic fields $\mu_0 H$ varying between –0.4 and +0.4 T. To dismiss possible magnetoresistive contributions to the measured signal, the antisymmetric part of ρ_{xy} under magnetic field reversal was considered according to the formula $\rho_H = \left[\rho_{xy}(+\mu_0 H) - \rho_{xy}(-\mu_0 H)\right]/2$. The Hall coefficient R_H was determined from the slope of the Hall resistivity ρ_H as a function of $\mu_0 H$ in the limit $\mu_0 H \longrightarrow 0$. Hall hole concentrations p_H and mobilities μ_H were inferred from the single-band formulas $p_H = r_H/R_H e$ and $\mu_H = R_H/\rho$, where e is the elementary charge and r_H is the Hall factor assumed to be equal to 1 in the present case. Deviations of r_H from unity will be discussed below based on theoretical results. The experimental uncertainty associated with low-temperature measurements of the electrical resistivity, thermopower, thermal conductivity and Hall coefficient are estimated to be 4%, 3%, 5% (below 200 K and 10% near 300 K) and 3%, respectively.

Thermopower and electrical resistivity were measured on bar-shaped samples with typical dimensions 1.5×1.5×7 mm^3 between 300 and 600 K using a ZEM-3 setup (Ulvac-Riko). Measurements performed upon heating and cooling did not show significant differences within experimental uncertainty (Figure S1 in SI), suggesting thermal stability up to at least 600 K.

The thermal conductivity was determined in the same temperature range by combining the thermal diffusivity a and specific heat C_p according to the relation $\kappa = aC_pd$ where d is the experimental density of the sample. a was measured on graphite-coated disc-shaped (parallel direction, 10 mm in diameter and 1 mm in thickness) and prism-shaped (perpendicular direction, 6×6×1 mm^3) samples by a laser flash technique using an LFA 427 instrument (Netzsch). As a first approximation, C_p was determined using the Dulong-Petit law. The temperature dependence of the density was neglected. The experimental uncertainties for the electrical resistivity, thermopower and thermal conductivity are estimated to be 5%, 5% and 10%, respectively, yielding a combined experimental uncertainty in the *ZT* values estimated to be 17%.[39]

2.8. Electronic Band Structure Calculations. Relaxation of the volume and atomic coordinates of $SnBi_2Te_4$ was performed with the Vienna *ab initio* simulation package (VASP).[40-44] Projector-augmented wave (PAW) pseudopotentials[45] with local density approximation (LDA) of Ceperley and Alder[46,47] as the exchange-correlation functional were used with a strict force convergence limit of 10^{-4} eV/Å and 10^{-6} eV for the self-consistent field (SCF) cycle convergence threshold. Monkhorst-Pack mesh of 15×15×15 **k**-points and plane-wave cutoff energy of 280 eV were used.

Further electronic structure calculations in the relaxed structure were performed using the all-electron full-potential linearized augmented plane wave (FP-LAPW) method, as implemented in the WIEN2k package,[48] with the modified Becke-Johnson (mBJ) semilocal exchange-correlation potential.[49] A dense grid with 50 000 **k**-points was used with spin-orbit coupling included. The energy convergence limit was set to 10^{-4} Ry. Valence and core separation was set to –6 Ry with muffin tin radii of 1.322 Å. Transport properties were calculated using the BoltzTraP code.[50]

3. RESULTS AND DISCUSSION

3.1. Electronic Band Structure. As a first step, structural relaxation of $SnBi_2Te_4$ was performed, with the experimental lattice parameters and atomic positions chosen as a starting point.[51] Although a possible mixing of Sn and Bi was suggested in prior studies,[33-35] a fully ordered structure was first considered in these calculations, each metalloid atom occupying only one crystallographic site (Table 1). The optimization process resulted primarily in a slight decrease in the *c* lattice parameter. For atomic positions that are not constrained by the symmetry, the changes were found to be negligible. Overall, the relaxed unit cell remains in good agreement with the experimental parameters.

Table 1. Results of structural optimization for $SnBi_2Te_4$. The Bi, Te1 and Te2 atoms are located at the 6*c* Wyckoff position of coordinates (0,0,*z*), while Sn is located at the 3*a* site (0,0,0).

	a,*b* (Å)	*c* (Å)	z_{Bi}	z_{Te1}	z_{Te2}
Experimental [11]	4.395(4)	41.606(2)	0.428(1)	0.135(9)	0.288(3)
Calculated	4.3712	40.6935	0.4273	0.1360	0.2887

Figure 2 shows the electronic band structure calculated along high symmetry points (see Figure S2 in the Supporting Information for a sketch of the Brillouin zone (BZ) with the location of the high-symmetry points). As Bi_2Te_3,[52] $SnBi_2Te_4$ has a multivalley band structure, where the valence band maximum (VBM) is located away from high symmetry points. This VBM is found in the Γ-Z-U-F plane ("mirror plane"), close to the L*-U direction. From the theoretical calculations using the mBJ exchange-correlation potential, $SnBi_2Te_4$ is a semiconductor with an indirect, narrow band gap of 45 meV, which is in good agreement with the experimental value of 50 meV reported in a prior study.[53] The conduction band minimum (CBM), on the other hand, lies along the Γ-Z direction.

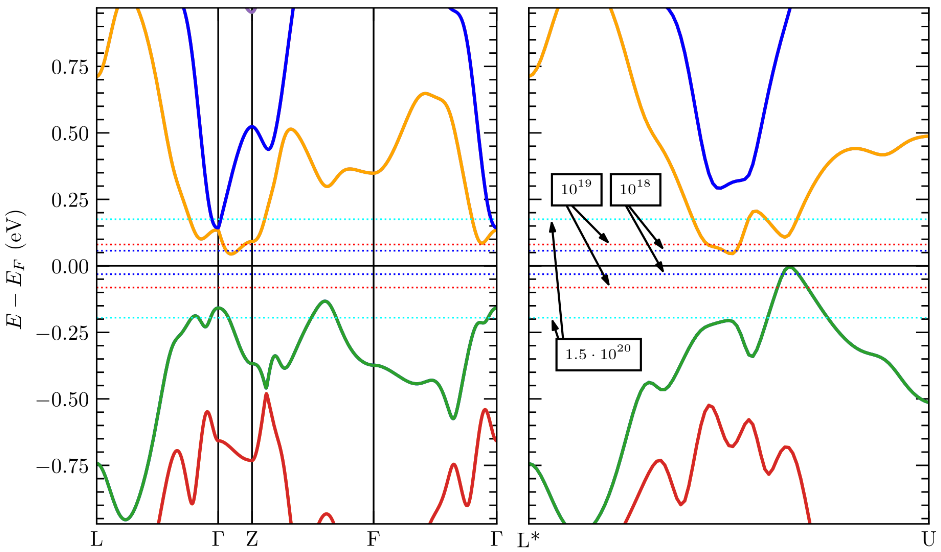

Figure 2. Electronic dispersion curves for $SnBi_2Te_4$. Horizontal dotted lines represent the Fermi level location for hole and electron concentrations of 10^{18} (dark blue), 10^{19} (red) and 1.5×10^{20} cm^{-3} (cyan).

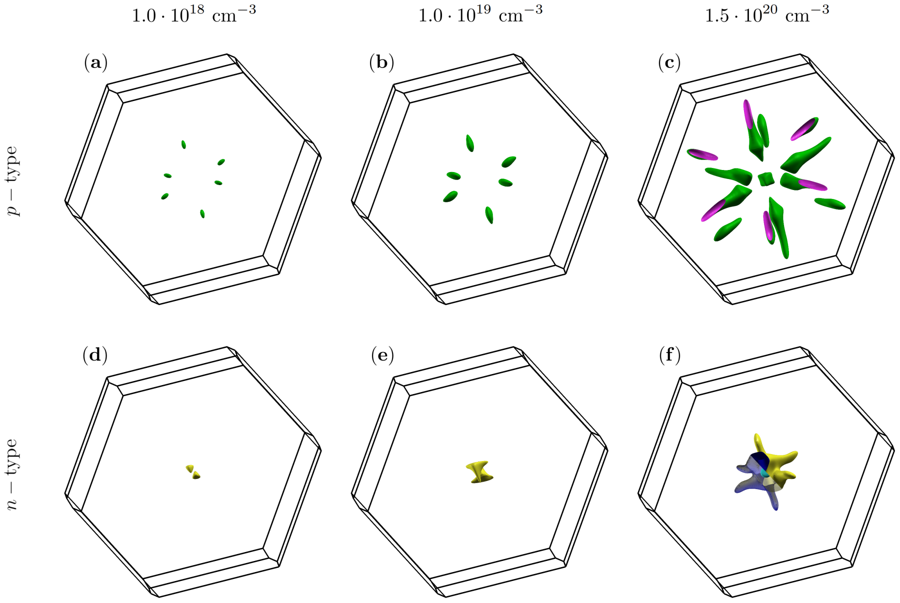

Figure 3. Fermi surfaces of *p*-type (a-c) and *n*-type (d-f) $SnBi_2Te_4$ for hole and electron concentrations of 10^{18}, 10^{19} and 1.5×10^{20} cm^{-3}.

The calculated Fermi surfaces (FS) of both *p*- and *n*-type $SnBi_2Te_4$ are presented in Figure 3 for three selected carrier concentrations. For hole-doped $SnBi_2Te_4$ at $p = 10^{18}$ cm^{-3}, six ellipsoidal pockets lie in the Γ-Z-U-L plane (Fig. 3a). With an increasing number of holes, the shape of those pockets remains mostly unchanged (Fig. 3b), becoming only slightly larger while pointing towards the U points in the BZ. Upon shifting the Fermi level (E_F) deeper inside the bands, multiple valence band maxima are crossed (e.g., Z-F or L-Γ in Fig. 2) leading to the appearance of additional pockets near the Z-U direction (Fig. 3c). In addition, a single pocket forms at the Γ point with a distinctive shape of two rotated tetrahedrons. Considering *n*-type $SnBi_2Te_4$ with low electron concentration (Fig. 3d), the FS consists of two small pockets along the Z-Γ-Z direction. In addition to the growth of these pockets, further doping leads to the formation of three flat surfaces in the Γ-Z-F-L plane (Fig. 3e). Finally, for $SnBi_2Te_4$ doped to $n = 1.5\times10^{20}$ cm^{-3}, those surfaces begin to form pipelike shapes in the Z-U direction. Previously-separated pockets now form one cylindrical sheet along the Z-Γ-Z direction. Furthermore, with E_F deeper into the CB, the second band is crossed, which appears as a single, small pocket centred at the Γ point (Fig. 3f).

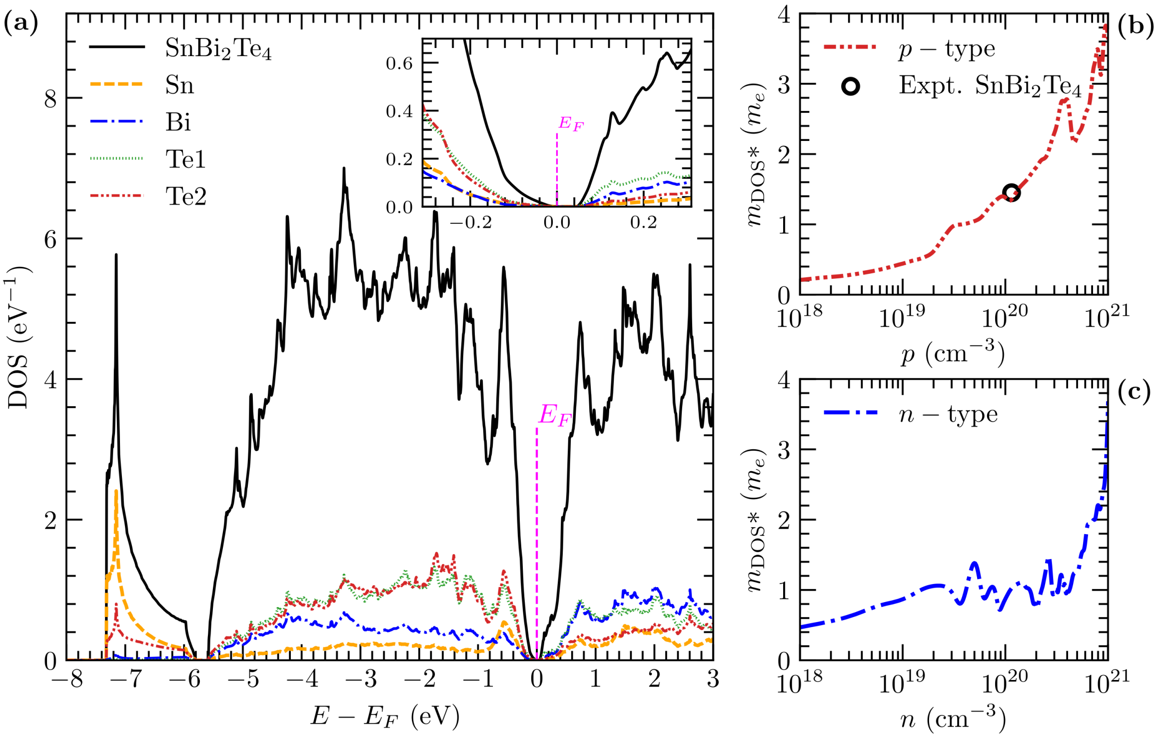

Figure 4. a) Electronic density of states (DOS) of SnBi$_2$Te$_4$ with atomic contribution. The inset shows a magnification in the energy range around the Fermi level E_F. Density-of-states effective mass m^*_{DOS} of charge carriers for b) p- and c) n-type SnBi$_2$Te$_4$.

The total and partial densities of states (DOS) of SnBi$_2$Te$_4$ are presented in Figure 4a (see Figure S3 in SI for the orbital decomposition of the DOS). The total DOS in the valence band is mainly formed by the Te 5p states, while the contribution from the Sn 5s and Bi 6p states is much lower. The DOS near the VB edge is relatively low, corresponding to a small density-of-states effective mass m^*_{DOS}, which was calculated with a method given in Ref. 54 and shown in Figures 4b and 4c as a function of the carrier concentration. For $p = 10^{18}$ cm^{-3}, $m^*_{DOS} = 0.2m_e$ (m_e is the bare electron mass) even though 6 FS pockets contribute to the DOS at this carrier concentration. This gives a small average single-pocket effective mass of $m^* = 6^{-2/3}m^*_{DOS} = 0.06m_e$, in agreement with the dispersive character of the valence band edge (see Fig. 2). The small band-effective mass can yield high carrier mobility, which together with a large valley degeneracy, is beneficial for thermoelectric properties. The structure of the valence bands is qualitatively similar to Bi_2Te_3, where 6 FS pockets also contribute to the transport at low hole concentrations.[52] However, m^*_{DOS} in $SnBi_2Te_4$ is lower than that observed in Bi_2Te_3, for which at the same hole concentration of 10^{18} cm^{-3} $m^*_{DOS} = 0.37m_e$.[53] m^*_{DOS} increases gradually in $SnBi_2Te_4$ with increasing p, and as the DOS rapidly rises below –0.1 eV (see Fig. 4a), m^*_{DOS} reaches $1.0m_e$ above 4×10^{19} cm^{-3} and $1.3m_e$ around 10^{20} cm^{-3}, in good agreement with the value determined from thermopower measurements, as discussed below. The conduction band, on the other hand, has a steeper DOS slope near the band edge, with a larger contribution from Bi states. This results in a heavier m^*_{DOS} near the band edge, with m^*_{DOS} ~$0.5m_e$ at $n = 10^{18}$ cm^{-3}. Two FS pockets contribute to this value, albeit with a much larger single-pocket average band mass of ~$0.31m_e$ that originates from flatter electronic dispersions (see Fig. 2). Thus, the structure of the conduction bands is different from Bi_2Te_3, for which the FS is composed of 6 pockets at $n = 10^{18}$ cm^{-3}, which evolves into 8 pockets around 5×10^{18} cm^{-3}.[53] The increase in m^*_{DOS} with n in $SnBi_2Te_4$ is then slower compared to the valence bands, with m^*_{DOS} remaining below $1.0m_e$ over a broader carrier concentration range. The calculated electronic structure agrees very well with those determined theoretically by DFT (Refs. 20, 21, 33, 34, 48, 50, 52-55) and experimentally by ARPES measurements.[50,55] Compared to available DFT studies,[20,55-58] only slight differences are observed, most likely due to calculation details.

Calculations of the transport properties (electrical conductivity, thermopower and power factor) were performed within the Boltzmann theory within the constant relaxation time approximation. Thus, both the electrical conductivity σ and the power factor PF depend linearly on the relaxation time. For this reason, a direct comparison with the experimental values is only possible for the thermopower, as the constant relaxation time is cancelled when α is calculated. Since $SnBi_2Te_4$ has a rhombohedral crystal structure, we analyse the diagonal elements of the tensors of the transport properties in the in-plane direction (denoted xx) and along the trigonal axis (denoted *zz*). Effective values of α, corresponding to a polycrystalline material, has been approximated using the parallel grain model[59]

$$\alpha_{eff} = \frac{\alpha_{xx}\sigma_{xx} + \alpha_{yy}\sigma_{yy} + \alpha_{zz}\sigma_{zz}}{\sigma_{xx} + \sigma_{yy} + \sigma_{zz}} \tag{1}$$

with $\alpha_{xx} = \alpha_{yy}$ and $\sigma_{xx} = \sigma_{yy}$ due to the rhombohedral symmetry of $SnBi_2Te_4$ (see Figure S4 in SI for the power factor, *PF*).

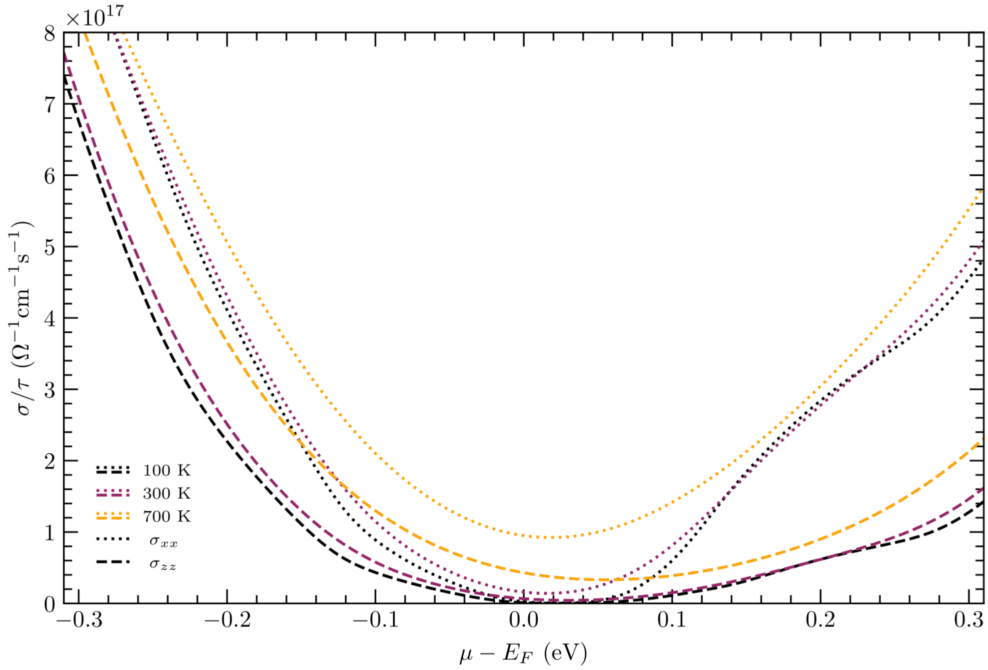

Figure 5. Calculated energy-dependent ratio of the electrical conductivity σ to the relaxation time τ for selected temperatures $T = 100$, 300 and 700 K as a function of the chemical potential μ. E_F corresponds here to the edge of the valence band.

Figure 5 shows the energy-dependent electrical conductivity over the relaxation time for $SnBi_2Te_4$ for three selected temperatures $T = 100$, 300 and 700 K. The σ_{xx} and σ_{zz} components of the transport function tensor are marked with dotted and dashed line, respectively (this convention will be also used for Figure 6 below). In these transport calculations, the band gap determined above (that is, 45 meV) was used. Overall, the transport function highly resembles the DOS plot, with significant anisotropy present. Considering a wide range of chemical potential, the σ_{xx} component dominates close to the valence band (VB) edge, especially at high temperatures. When sufficiently far away from VB, the situation is inverted ($\sigma_{zz} > \sigma_{xx}$). Furthermore, in n-type $SnBi_2Te_4$, a steep slope of σ_{xx} is visible between 0 and 0.4 eV, which results in high α_{xx} at low carrier concentrations (see Fig. 6) as $\alpha \propto d(\ln\sigma)/dE$.

The results of calculations of α are shown in Figure 6 for both p- and n-type $SnBi_2Te_4$. The variations in the carrier concentration were simulated by a rigid shift of the Fermi level. Starting with the hole-doped variant, the maximum value of the effective thermopower α_{eff} is about 175 – 180 μV K^{-1}. At lower temperatures (100 and 300 K), the anisotropy is weak, being only important at 300 K below 10^{19} cm^{-3} where the α_{zz} component dominates. Stronger anisotropy is present in the whole concentration range at 700 K. Anisotropy is more prominent for n-type, but with a reverse dominant direction at lower carrier concentration. The α_{xx} component is higher at low concentration range, while above ~10^{20} cm^{-3}, α_{zz} outweighs α_{xx}. At 300 K, we observe similar absolute maximum values of α_{eff} ~ 190 μV K^{-1}, as in the p-type analogue, although at a much higher carrier concentration (2×10^{19} compared to 5.3×10^{18} cm^{-3}). Because of the asymmetry of effective masses and conductivity, bipolar effect is much stronger in the n-type region, especially along the z axis. Upon increasing temperature, a strong bipolar effect occurs in electron-doped $SnBi_2Te_4$, suppressing the maximal α_{eff} at high temperatures down to approximately –150 μV K^{-1} at 700 K. A comparison of the calculated and measured α values is shown in Table 2.

Table 2. Comparison of the experimental (perpendicular direction) and calculated values of α in μV K^{-1} at 300 K for carrier concentrations of 1.11±0.03×10^{20} cm^{-3} ($Sn_{0.95}Bi_2Te_4$) and 1.56±0.05×10^{20} cm^{-3} ($SnBi_2Te_4$). Theoretical results include values for nominal carrier concentrations as well as corrected for the two possible Hall factors.

		$Sn_{0.95}Bi_2Te_4$			$SnBi_2Te_4$		
Experimental values		119.9±3.6			103.0±3.1		
		α_{eff}	α_{xx}	α_{zz}	α_{eff}	α_{xx}	α_{zz}
Calculated $SnBi_2Te_4$	Nominal	93.5	90.0	105.3	83.5	79.7	96.3
	‘in-plane' Hall factor	97.9	94.5	109.3	87.7	84.0	100.1
	‘trigonal’ Hall factor	121.2	118.7	129.5	112.1	109.2	121.8

The comparison with the experimental results (measured at T = 300 K) shows that our calculations agree well with experimental data available in the literature for both n- and p-type doped $SnBi_2Te_4$,[30,31,36,37] despite the approximation of constant relaxation time. Of note, the experimental data points were placed assuming that the Hall carrier concentration equals the nominal one. However, the concentrations obtained from the formula $p_H = 1/R_H e$ probably overestimate the actual ones as discussed below. Thus, the experimental data points can be seen as shifted towards the right in the figure with respect to the calculated lines. For n-type samples, a slight underestimation of the thermopower of about 20 μV K^{-1} occurs from n = 5×10^{19} to n ~ 1.5×10^{20} cm^{-3}. This difference is however not surprising as n-type samples were only obtained upon heavy-alloying on the Sn site with Pb.[30,31]

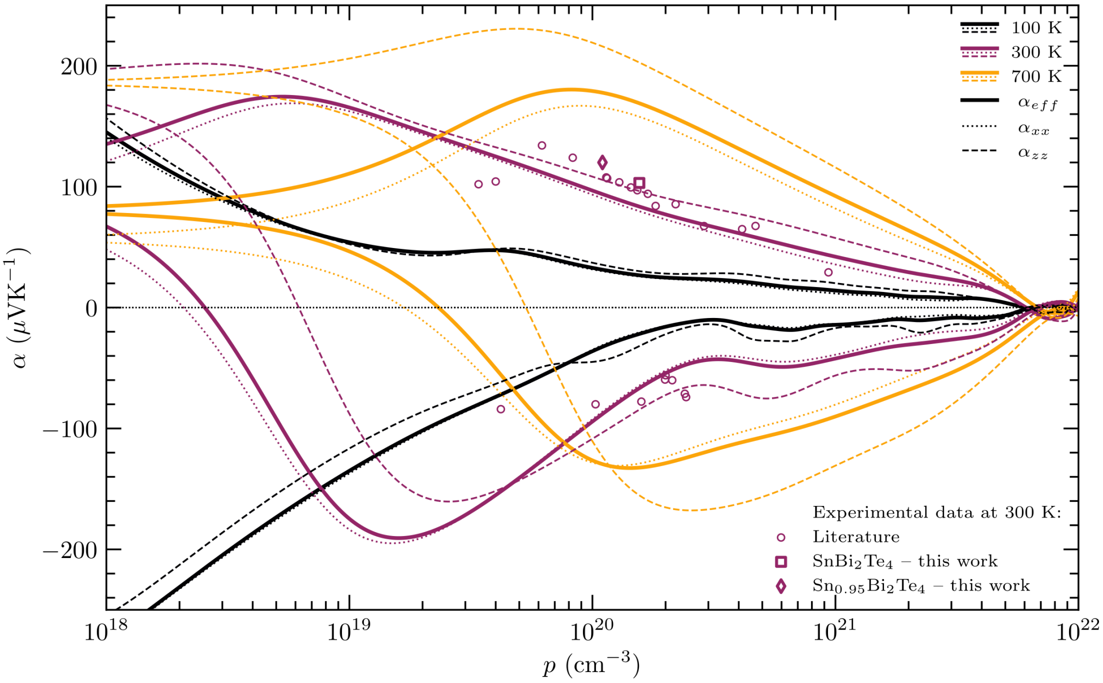

Figure 6. Calculated thermopower α as a function of carrier concentration at T = 100, 300 and 700 K. Experimental data from literature have been collected from Refs 29, 30, 31, 36, 37, 60 and 61.

To be able to compare more precisely the results of calculations with the experimental values, the Hall coefficient tensor R_H^{ijk} was analyzed. The indexes i, j and k refer to the direction of the current, Hall voltage and magnetic field, respectively. The Hall carrier concentrations ($p_H^{ijk} = 1/eR_H^{ijk}$), calculated from the two independent components of R_H^{ijk}, are shown as a function of the ‘true’ nominal carrier concentration in Figure 7. In the rhombohedral (hexagonal) symmetry, there are two independent Hall coefficients, for the in-plane (*x*,*y*) and trigonal (*z*) magnetic field directions. Within the experimentally-accessible p range, a significant anisotropy is present, similar to what has been observed for the electrical conductivity, with the p_H^{xyz} component (that is, with the magnetic field along the trigonal axis) visibly deviating from the $x = y$ line. As a result, the Hall carrier concentration inferred from Hall effect measurements performed in this geometry may be significantly different from the nominal one and a correction (the so-called Hall factor r_H) should be used $p_H = r_H/eR_H$. In the present case, as discussed in the experimental part below, polycrystalline samples are textured, even though the degree of anisotropy remains moderate. The Hall measurements were performed with the current flowing along the direction perpendicular to the pressing direction and the magnetic field along the pressing direction.

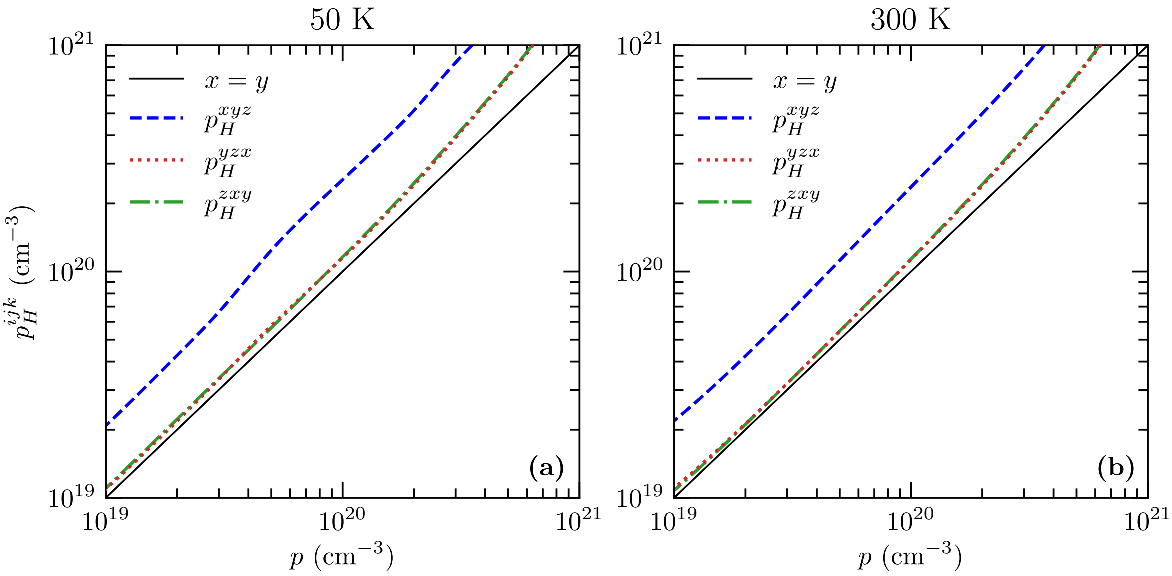

Figure 7. Hall carrier concentration $p_H^{ijk} = 1/eR_H$ for 50 K (left panel) and 300 K (right panel) as a function of the nominal carrier concentration p for p-type SnBi$_2$Te$_4$. The indexes i, j, k refer to the direction of the current, voltage, and magnetic field, respectively.

The anisotropy of the measured electrical resistivity (larger in the direction parallel to the pressing direction) suggests that the orientation of crystallites with the trigonal axis along the SPS direction was dominating, as in the calculations $\frac{1}{\sigma_{zz}} > \frac{1}{\sigma_{xx}}$. Thus, the measured Hall resistivity represents mostly the p_H^{xyz} component of the Hall resistivity tensor, for which the calculated Hall factor is as low as 0.402 (that is, the experimental Hall carrier concentration with no applied Hall factor overestimates the nominal values by 250%). On the other hand, for the magnetic field oriented along the in-plane direction, this effect would be much weaker, with a calculated $p_H^{yzx} = p_H^{zxy}$ Hall factor of 0.866. Thus, the representative value for textured polycrystalline samples should fall between these two limits. However, with a tendency of preferred alignment of basal planes perpendicular to the pressing direction, our samples should be closer to the p_H^{xyz} limit. Even though the measured thermopower (see below) shows a moderate level of anisotropy in agreement with the calculations presented above, the predicted anisotropy of the Hall resistivity makes the comparison of the experimental and theoretical data more difficult due to the sensitivity on the assumed carrier concentration. In Table 2, we have included the values of the average thermopower obtained by correcting the experimental Hall carrier concentration with these two limits of the Hall factor, with the experimental results falling in between.

3.2. Crystal Structure and Phase Purity of Polycrystalline Samples. $SnBi_2Te_4$ crystallizes with a layered, anisotropic unit cell described in the rhombohedral space group $R\bar{3}m$ (see Fig. 1).[29,32,36] The crystal structure consists of a stacking along the *c* axis of seven-layer building blocks forming an infinite 7–7 sequence, which can be viewed as the insertion of an additional layer of Sn-Te octahedra into the quintuple layers that are characteristic of Bi_2Te_3. In a perfectly-ordered structure, each Sn atom occupy nearly-symmetrical octahedra (3*a* Wyckoff site) formed by six Te1 atoms with Sn-Te interatomic distances (3.16 Å) very close to those observed in the binary $Sn_{1-\delta}Te$ (3.14 Å).[36,62] Bi atoms occupy slightly-distorted octahedra (6*c* Wyckoff site), due to the $6s^2$ Bi lone pair, formed by three Te1 and three Te2 atoms.[36,62] The corresponding interatomic distances Bi-Te1 and Bi-Te2 of 3.32 and 3.05 Å, respectively, are close to those characterizing Bi_2Te_3 (3.24 and 3.04 Å, respectively). The close agreement between the atomic environments of Sn and Bi in $SnBi_2Te_4$ and those in their respective parent compounds $Sn_{1-\delta}Te$ and Bi_2Te_3 suggests an ordered structure. In contrast to these crystallographic considerations, some experimental evidence based on Mössbauer spectroscopy on polycrystalline $SnBi_2Te_4$ specimens have suggested a mixed occupancy of Sn/Bi, with 33%

of Sn atoms occupying the Bi site.[35,57] This picture may be supported by the small difference in electronegativity between Sn and Bi (1.96 and 2.02 on the Pauling scale, respectively). Nevertheless, both $SnBi_2Te_4$ and its sister compound $SnSb_2Te_4$ have been suggested to be the two members of the $(A^{IV}Te)_n(Bi_2X_3)_m$ family exhibiting the least cation exchange, based on resonant synchrotron X-ray diffraction for the latter.[63] While the presence of Sn_{Bi} antisite defects that contribute one hole per defect possibly explains the intrinsic heavily-doped *p*-type nature of $SnBi_2Te_4$, their concentration remain to be determined.

To further investigate the possible presence of a statistical distribution of Sn and Bi on the 3*a* and 6*c* sites, ^{119}Sn Mössbauer spectroscopy experiments were performed at 15 K to probe the chemical environment of Sn atoms. The experimental Mössbauer spectrum (Figure 8 and Figure S5 in SI) evidences the presence of two components. The weak one, on the left part of the spectrum, is characterized by an isomer shift (IS) of 0.08±0.04 mm s^{-1} with respect to $BaSnO_3$ at room temperature and a quadrupole splitting (QS) of 0.54±0.04 mm s^{-1}. It corresponds to a Sn^{4+} oxidation state and can be ascribed to the presence of a minute amount of SnO_2, whose literature hyperfine parameters are respectively IS = 0±0.03 mm s^{-1} at 300 K and 0.06±0.01 mm s^{-1} at 4.2 K, and QS = 0.58±0.04 mm s^{-1}.[64,65]

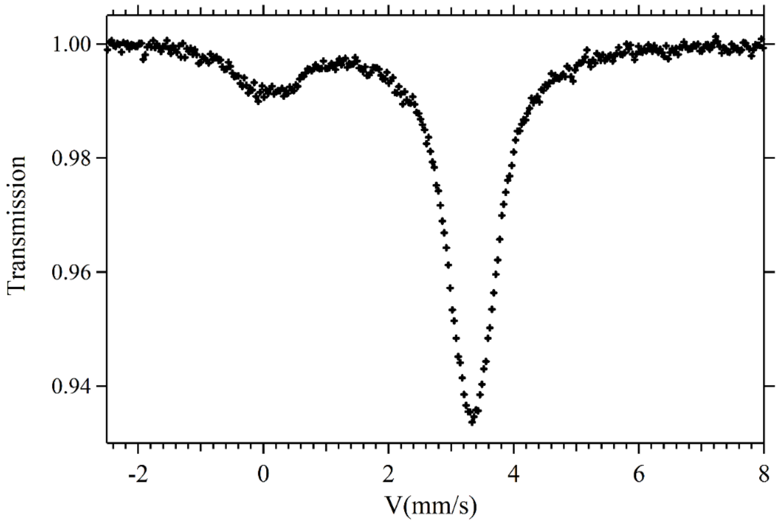

Figure 8. ^{119}Sn Experimental spectrum of $SnBi_2Te_4$ at 15 K. The broadened component close to 0 mm s^{-1} is attributed to SnO_2.

The minimum of the main symmetrical component is at 3.34±0.04 mm s^{-1} associated with Sn^{+2} oxidation states, which is consistent with charge balance according to the ionic formula $Sn^{2+}(Bi^{3+})_2(Te^{2-})_4$. Various fits were attempted with either a single peak or with a sum of a single peak and of a doublet as considered in a prior ^{119}Sn Mössbauer study at 77 K.[35] The single peak and the doublet have the same isomer shifts within experimental errors (IS = 3.34±0.04 mm s^{-1}). This IS differs from that (IS = 3.50±0.04 mm s^{-1}) reported in this previous study.[35] This difference is too large to be solely attributed to the difference of the recording temperatures (15 and 77 K). Usually, the velocity scale is calibrated from the room-temperature spectrum of *bcc* Fe as performed herein and in Ref. 35. However, the origin of the velocity scale must still be determined. Here, this origin was determined from a ^{119}Sn spectrum of $BaSnO_3$. This correction yields a shift of –0.09 mm s^{-1} of the Fe scale. The above-mentioned hyperfine parameters of SnO_2 provide a test of its correctness herein.

While using a single peak yields a good fit, in spite of visible deviations around the peak maximum and in the tails, the best fits are obtained by considering both a singlet and a doublet. However, the weight of each contribution cannot be unequivocally determined from the measured signal, with various ratios providing fits of similar qualities (Figure S5 in SI). Therefore, a firm conclusion about their respective weight cannot be reached. This limitation is intrinsic to the shape of the main peak and is not a consequence of the counting statistics (see the additional discussion and Figure S6 in the SI where the dependence of the fitted quadrupole splitting QS(*p*) of the doublet when the singlet is assumed to originate from a proportion of Sn atoms *p* is shown). These findings nevertheless indicate that Sn_{Bi} antisite defects exist in $SnBi_2Te_4$, in agreement with prior studies.[23,35-37]

The PXRD patterns of the $SnBi_2Te_4$ and $Sn_{0.95}Bi_2Te_4$ samples collected after annealing for 10 days (for sake of completeness, diffraction patterns collected on samples before annealing are shown in Figure S7 in SI) and of $SnBi_2Te_4$ after annealing for 75 days can be well indexed to the theoretical diffraction pattern of ordered $SnBi_2Te_4$ (structural model COD1520774), suggesting the absence of secondary phases within the detection limit of this technique (Figure 9). Rietveld refinements were performed by considering an ordered model (Figures S8 to S10 in SI), giving lattice parameters a = 4.398(1) Å and c = 41.615(1) Å for $SnBi_2Te_4$ (a = 4.3995(1) Å and c = 41.603(1) Å for the sample annealed 75 days) and a = 4.399(1) Å and c = 41.602(2) Å for $Sn_{0.95}Bi_2Te_4$. Attempts at refining the concentration of Sn on the Bi site were inconclusive, as the final stoichiometry does not match the chemical composition measured by EPMA (see below), as discussed previously.[36] While a model considering Sn/Bi mixing improves the description of low-intensity diffraction peaks, the presence of a slight renormalization of the peak intensities due to the anisotropic crystal structure of $SnBi_2Te_4$, make it difficult to disentangle the contribution of both effects on the measured signal. This is demonstrated by additional XRD data collected on consolidated bulk pieces cut parallel and perpendicular to the pressing direction (Figure S11 in SI).

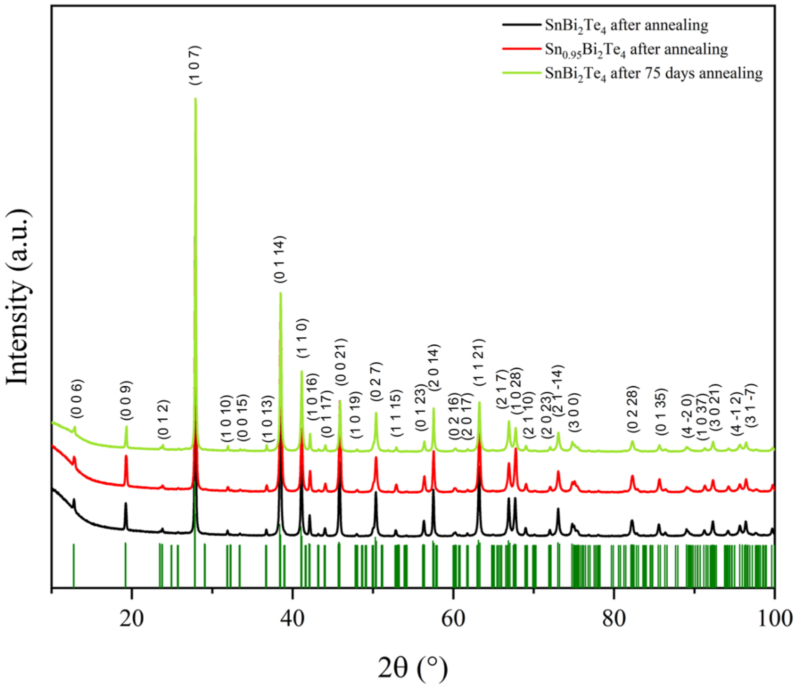

Figure 9. Powder X-ray diffraction patterns of $SnBi_2Te_4$ and $Sn_{0.95}Bi_2Te_4$ annealing for 10 days and of $SnBi_2Te_4$ annealed for 75 days. The theoretical PXRD pattern is also shown for comparison (green vertical ticks). The main reflections are indexed.

SEM images in backscattered electron (BSE) mode and the corresponding elemental mapping from EDXS show that all the elements are homogeneously distributed, without any evident secondary phase observable at this scale (Figure S12 in SI). The average chemical compositions determined by EPMA are $Sn_{0.99(1)}Bi_{2.00(1)}Te_{4.01(1)}$ and $Sn_{0.98(1)}Bi_{2.02(1)}Te_{3.99(1)}$ for $SnBi_2Te_4$ and $Sn_{0.95}Bi_2Te_4$, respectively. While these results indicate that the actual composition of $SnBi_2Te_4$ matches the nominal one to within experimental uncertainty, a larger difference is observed for $Sn_{0.95}Bi_2Te_4$ for which the actual Sn atomic content is clearly higher than the nominal one. This suggests that only a narrow compositional window exists around the stoichiometric composition $SnBi_2Te_4$. According to the $Sn_{1-\delta}Te$–Bi_2Te_3 pseudo-binary phase diagram,[32] the strong off-stoichiometry used in the nominal composition of $Sn_{0.95}Bi_2Te_4$ is expected to give rise to the formation of $SnBi_2Te_4$ as the main phase with a small fraction of the $SnBi_4Te_7$ compound. The presence of $SnBi_4Te_7$ is however not observed in the PXRD pattern, with its characteristic (005) reflection at 18.4° being well separated from the (009) reflection of $SnBi_2Te_4$ at 19.1°. Hereafter, we will use for clarity the EPMA compositions to label these two samples.

The presence of this secondary phase as well as the crystal structure of both samples were further investigated at the atomic scale by transmission electron microscopy (TEM). The expected infinite sequence of septuple layers stacked along the *c* axis, experimentally evidenced on nanoplates of $SnBi_2Te_4$,[57] is observed in the sample annealed for 75 days, as shown by typical STEM images taken along the [100] direction (Figure 10). Similar analyses performed on the samples annealed for 10 days reveal a more complex situation, with the presence of a large number of stacking faults (see Figures S13 to S15 and additional discussion in SI). This stacking complexity can be viewed as an incommensurate modulation along the *c* axis, possibly being fully disordered or forming a composite structure that can be represented as several intergrown sublattices, similar to what has been observed in several other homologous series such as $(Bi_2)_n(Bi_2X_3)_m$ (X = Se or Te) or $(GeTe)(Bi_2Te_3)_n$.[66-68] The main reason for the lack of long-range stacking ordering in $Sn_{0.99(1)}Bi_{2.00(1)}Te_{4.01(1)}$ and $Sn_{0.98(1)}Bi_{2.02(1)}Te_{3.99(1)}$ is thus the annealing time being too short to obtain a fully-ordered structure. In comparison, annealing only three days was reported to be sufficient to obtain a well-ordered structure at the atomic level in $GeBi_2Te_4$,[69] suggesting distinct formation kinetics depending on the nature of the A^{IV} cation. Additional TEM-EDXS mappings (Figure S16 in SI) confirms an overall homogeneous spatial distribution of the three elements in most areas of the samples, with small regions where Sn excess is observed. In $Sn_{0.98(1)}Bi_{2.02(1)}Te_{3.99(1)}$, Te-rich regions, possibly related to the binary $Sn_{1-\delta}Te$ present before annealing (see Figure S7 in SI), are also observed (Figure S16j in SI).

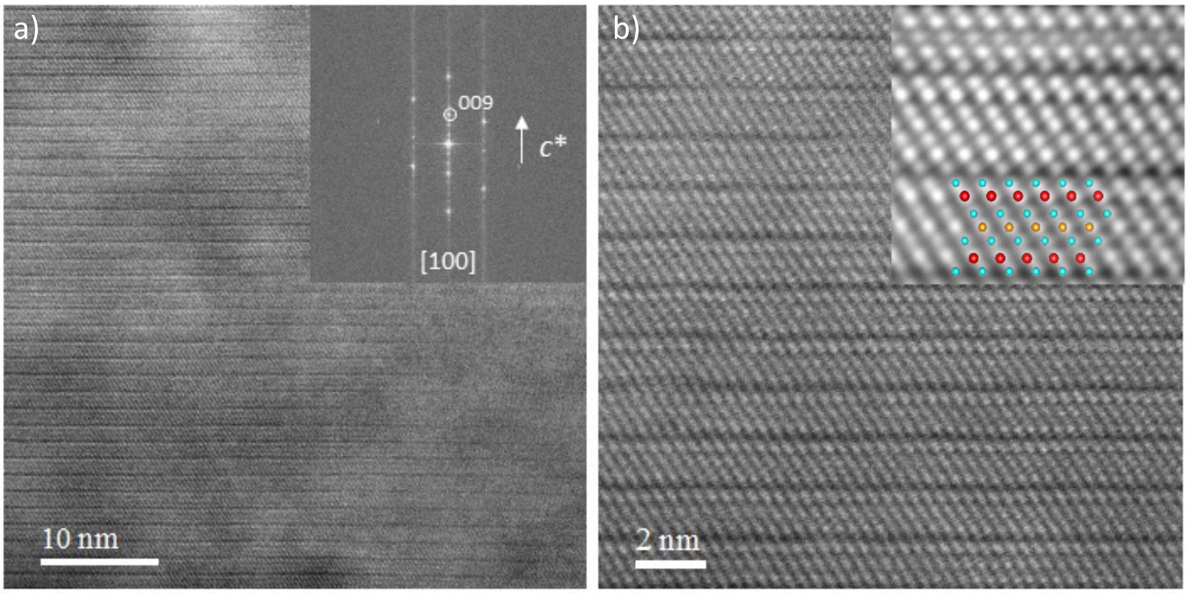

Figure 10. STEM images on a $SnBi_2Te_4$ sample annealed for 75 days. The inset in panel a) shows the corresponding electron diffraction pattern. In panel b), the inset shows the inverse fast-Fourier transform (IFFT) of a fragment of the STEM image with a septuple layer overlaid.

3.3. Transport Properties. The temperature dependence of the electrical resistivity ρ and thermopower α measured perpendicular and parallel to the pressing direction for $Sn_{0.99(1)}Bi_{2.00(1)}Te_{4.01(1)}$ and $Sn_{0.98(1)}Bi_{2.02(1)}Te_{3.99(1)}$ are shown in Figures 11a and 11b. For comparison purposes, the results reported in Ref. 36 have been added. The comparison of the transport properties measured for $Sn_{0.99(1)}Bi_{2.00(1)}Te_{4.01(1)}$ and for the sample annealed for 75 days are shown in Figure S17 in the SI. For both samples annealed for 10 days, $\rho(T)$ has a positive temperature dependence, characteristic of degenerate semiconducting behavior with room-temperature values of 10.9±0.4 and 12.6±0.5 μΩ m for $Sn_{0.99(1)}Bi_{2.00(1)}Te_{4.01(1)}$ and $Sn_{0.98(1)}Bi_{2.02(1)}Te_{3.99(1)}$, respectively. The difference in the ρ values between the parallel and perpendicular directions remains relatively small, amounting to at most ~15%, in spite of the layered crystal structure of $SnBi_2Te_4$. $\alpha(T)$ increases nearly linearly up to about 300 K where values of 105±3.1 and 120±3.6 μV K^{-1} are achieved for $Sn_{0.99(1)}Bi_{2.00(1)}Te_{4.01(1)}$ and $Sn_{0.98(1)}Bi_{2.02(1)}Te_{3.99(1)}$, respectively. The higher α values achieved in $Sn_{0.98(1)}Bi_{2.02(1)}Te_{3.99(1)}$ compared to $Sn_{0.99(1)}Bi_{2.00(1)}Te_{4.01(1)}$ suggests close, yet slightly different Sn deficiencies. However, the fact that the nominal Sn-deficient sample shows higher α values indicates a lower p_H, contrary to the nominal composition for which the reduced Sn content is expected to increase p_H due to the acceptor-like nature of Sn vacancies. This trend is consistent with the TEM analyses revealing the presence of intergrown $SnBi_4Te_7$, indicating that a large concentration of Sn vacancies cannot be accommodated in $SnBi_2Te_4$. α remains positive over the entire temperature range indicative of p-type behavior, in agreement with prior studies.[29,36] Upon warming, an intrinsic regime of conduction sets in around 350 K, evidenced by decreased ρ and α values due to the thermal activation of minority carriers across the electronic band gap. Compared to previous studies,[29,36] the maximum α values are shifted towards lower temperatures, suggesting that our two samples have lower hole concentrations. Interestingly, all these characteristics remain similar in the sample annealed for 75 days, indicating that the disordered or ordered character of the septuple layers plays a secondary role in the transport properties. This might be due to the inherent disorder in the crystal structure induced by the Sn_{Bi} antisites that would mostly dominate the transport properties over the additional stacking disorder.

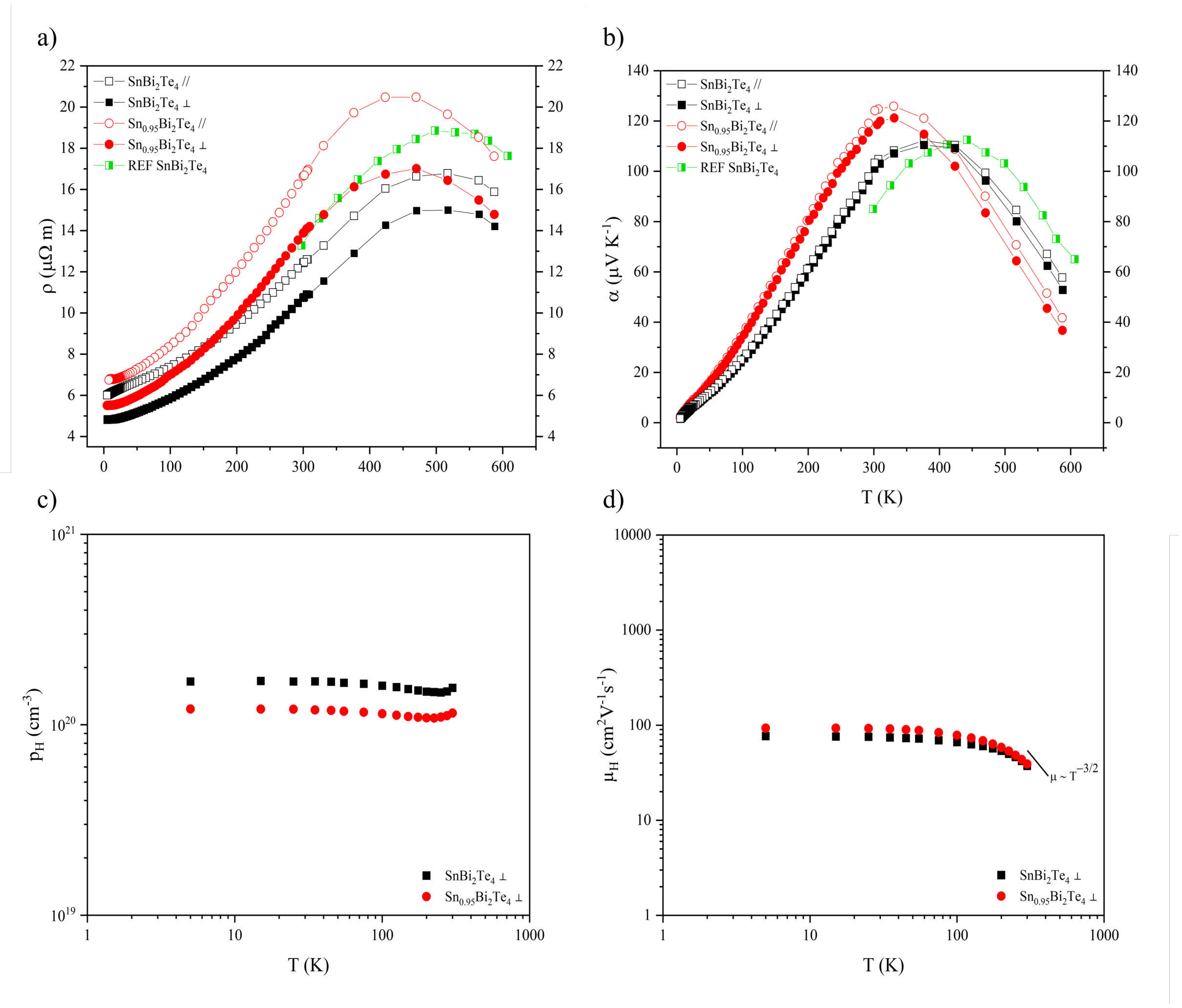

Figure 11. Temperature dependence of the a) electrical resistivity ρ, b) Seebeck coefficient α, c) hole concentration p_H and d) Hall mobility μ_H. In panels a and b, the data from Ref. 36 have been added for comparison.

The Goldsmid-Sharp relation,[70] $E_g = 2e\alpha_{max}T_{max}$, that relates the band gap E_g to the maximum values α_{max} reached at T_{max} (110±5.5 μV K^{-1} at 376 K for $SnBi_2Te_4$), yields an E_g value of 83±4 meV. Although this value is in fair agreement with the experimental value of 50 meV derived from ARPES measurements[53,58] and with our calculated value of 45 meV, the calculated temperature dependence of α (Figure 12) significantly deviates from the experimental one, with the bipolar effect predicted to occur above 600 K, at odds with the experimental maximum reached around 350 K.

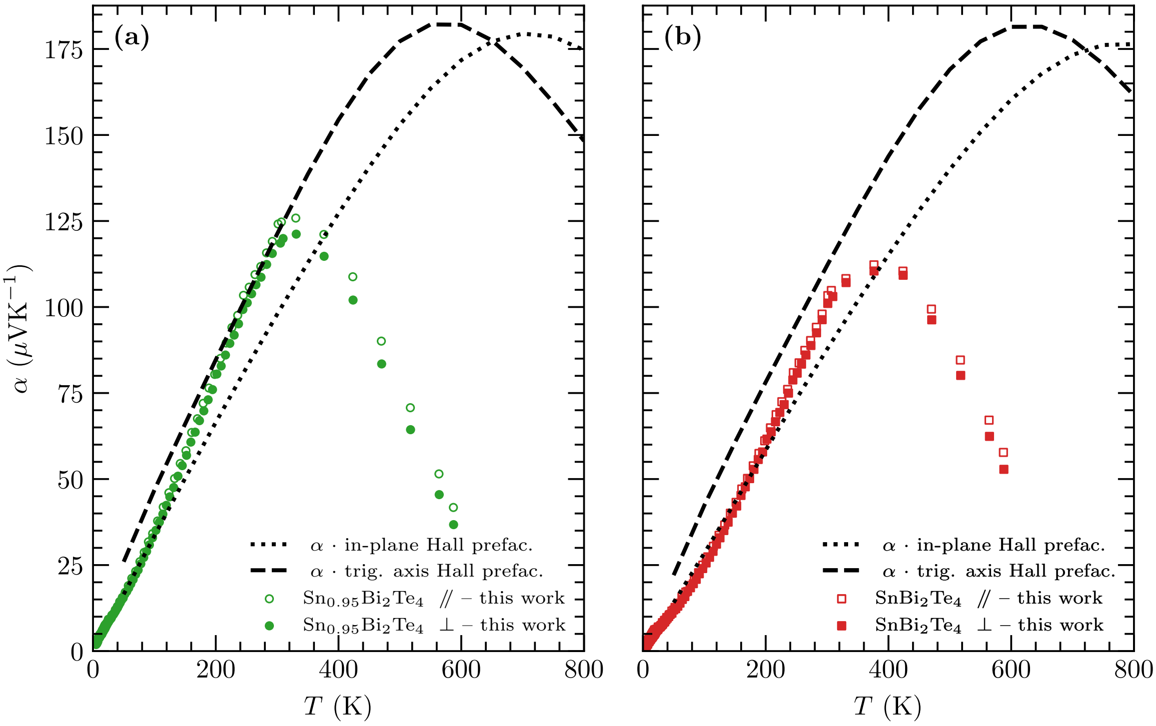

Figure 12. Calculated thermopower α as a function of temperature for the nominal carrier concentration corrected for the two Hall factors and compared to the experimental data (the ’in plane’ and ‘trigonal’ Hall factors refer to the magnetic field direction as discussed in the theoretical part, with the trigonal one expected to be closer to the experimental values). The Hall carrier concentrations of $Sn_{0.95}Bi_2Te_4$ (1.11±0.03×10^{20} cm^{-3}) and $SnBi_2Te_4$ (1.56±0.05×10^{20} cm^{-3}) were used in panel a) and b), respectively.

This difference reflects the inaccuracy of the estimation of E_g based on the Goldsmid-Sharp relation, which is valid only for non-degenerate semiconductors with no asymmetry between the conduction and valence band mobilities. The estimation from the calculated peak α value of about 175±8.8 μV K^{-1} at 600 K would yield a band gap greater than 210±10 meV, that is, more than 4.5 times larger than the value used in these calculations (45 meV). This can be attributed to the large asymmetry of the mobility between the valence and conduction bands (Figure S18 and S19 in SI).[71] If this 4.5-times overestimation of E_g is applied to the 83±4 meV value extracted from our measurements, the actual band gap of $SnBi_2Te_4$ is estimated to be less than 20 meV. To determine whether this explains the difference in the $\alpha(T)$ behavior, we have reduced twice the band gap value and recalculated $\alpha(T)$ for $E_g = 23$ meV. This effect alone is still not sufficient to explain the onset of the bipolar conduction, as the calculated α values do not match the measurements (Figure S20 in SI). Considering the Mössbauer spectroscopy results, we have tested whether the presence of antisite defects is at the origin of this behavior by comparing two models, a first one with Sn on Bi sites and a second one with Bi on Sn sites. Figure 13 shows the results for the first model, where a supercell of $Sn_{12}Bi_{24}Te_{48}$ was created and a single Bi atom was replaced by Sn (this yields the stoichiometry of $Sn_{12}(Bi_{23}Sn)Te_{48}$ = $Sn(Bi_{1.958}Sn_{0.042})Te_4$, that is, 4.2% of Sn_{Bi} antisite defects). The calculated density of states near the band gap is shown in the left panel. The Sn_{Bi} antisite defects visibly reduce the band gap to 16 meV, modify the shape of the DOS curve, and push the Fermi level deeper into the valence bands due to their acceptor-like character. The calculated DOS effective mass for the hole concentration of ~10^{20} cm^{-3} remains similar to the experimental estimate with a value of $1.1m_e$. However, the effect on the temperature dependence of α is very strong above 300 K, as seen in the two right panels of Figure 13. As previously, α is presented for the two possible corrections of the hole concentration between the Hall and nominal values (here the Hall factors near 10^{20} cm^{-3} are 0.16 and 1.22 for the trigonal and in-plane magnetic field directions, respectively, see

Table 3). With the assumption of the 'trigonal' Hall factor, the temperature dependence of α is very well described, especially the onset of the bipolar effect. For temperatures above 400 K, the larger deviation between calculations and measurements can be attributed to the growing importance of electron-phonon scattering, neglected in the constant relaxation time approximation.

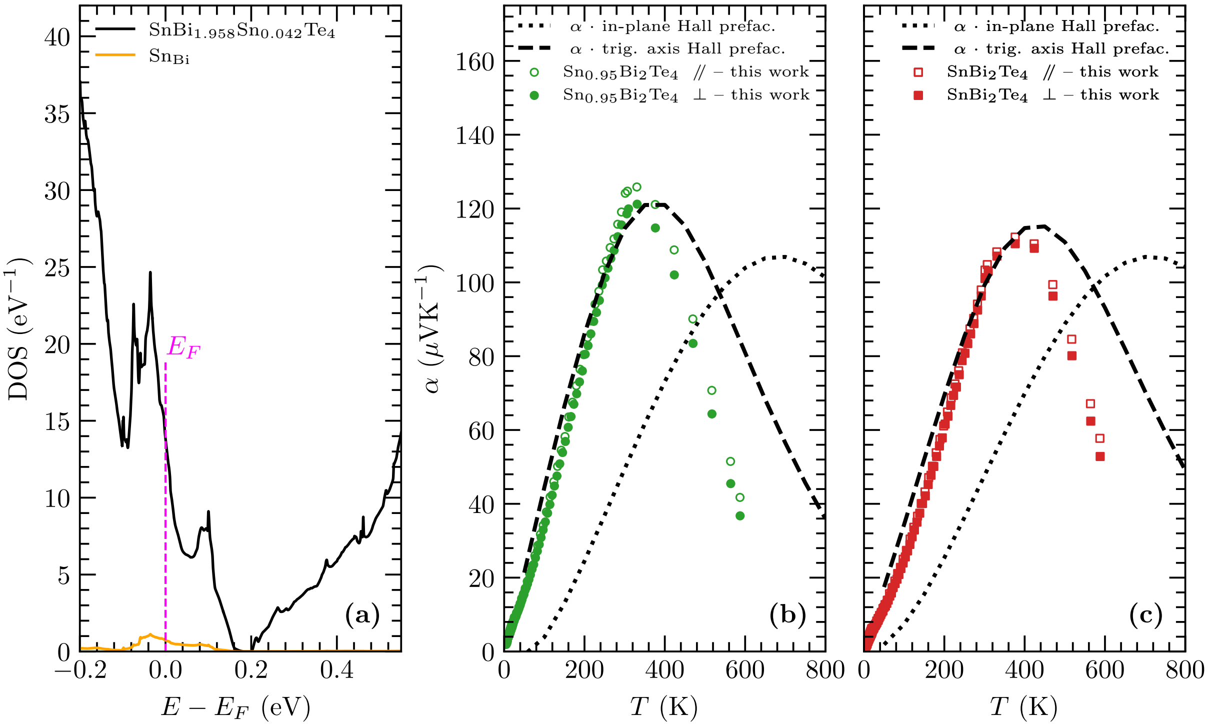

Figure 13. Panel a): Electronic density of states (DOS) of supercell Sn$_{12}$(Bi$_{23}$Sn)Te$_{48}$ = Sn(Bi$_{1.958}$Sn$_{0.042}$)Te$_4$. Panels b) and c): Comparison of the experimental and calculated thermopower α of the supercell at the nominal carrier concentrations obtained from Hall effect measurements with the two possible Hall factors as a function of temperature for b) Sn$_{0.95}$Bi$_2$Te$_4$ (that is, Sn$_{0.98(1)}$Bi$_{2.02(1)}$Te$_{3.99(1)}$) and c) SnBi$_2$Te$_4$ (that is, Sn$_{0.99(1)}$Bi$_{2.00(1)}$Te$_{4.01(1)}$).

Table 3. Comparison of the experimental (perpendicular direction) and calculated (supercell $Sn_{12}(Bi_{23}Sn)Te_{48}$) values of α in μV K^{-1} at 300 K for experimental carrier concentrations of $1.11\pm0.03\times10^{20}$ cm^{-3} ($Sn_{0.98(1)}Bi_{2.02(1)}Te_{3.99(1)}$) and $1.56\pm0.05\times10^{20}$ cm^{-3} ($Sn_{0.99(1)}Bi_{2.00(1)}Te_{4.01(1)}$) assuming the presence of a small concentration of Sn_{Bi} antisite defects.

		$Sn_{0.95}Bi_2Te_4$			$SnBi_2Te_4$		
Experimental values		119.9±3.6			103.0±3.1		
		α_{eff}	α_{xx}	α_{zz}	α_{eff}	α_{xx}	α_{zz}
Calculated $SnBi_{1.958}Sn_{0.042}Te_4$	Nominal	88.7	90.4	27.4	67.3	68.7	22.3
	'in-plane' Hall factor	49.4	48.3	64.7	47.7	45.1	81.1
	'trigonal' Hall factor	114.6	119.6	76.0	99.3	104.2	57.3

The second possibility of Bi_{Sn} antisite defects also leads to the shrinkage of the band gap to about 18 meV, as obtained for the $Bi_{0.083}Sn_{0.917}Bi_2Te_4$ supercell. However, for this case, the modifications mostly concern the conduction band DOS. Bi_{Sn} defects are also electrically active but behave as electron donors, leading to a predicted thermopower being in worse agreement with the experimental results (Figure S21 in SI). In addition, according to our calculations, the third possible type of defects, that is Sn vacancies, as in $Sn_{1-\delta}Te$,[72] only leads to rigid-band-like shift of the Fermi level position deeper inside the valence bands, with no significant changes of the electronic band structure of $SnBi_2Te_4$ (see Figure S22 in SI). Thus, it also cannot explain the experimentally observed behavior of $\alpha(T)$. These findings show that Sn_{Bi} antisite defects are the dominant defects in $SnBi_2Te_4$, which have a significant impact on the thermoelectric properties by shifting the onset of bipolar conduction towards lower temperatures, a detrimental effect for mid-temperature range applications. In addition to the reduction of the band gap, the presence of these defects changes the mobility ratio (see Figure S18 in SI), promoting stronger bipolar effects in p-type samples. The calculated mobility ratio (within the constant relaxation time approximation) between holes and electrons drops below 1.0 if the Fermi level is located deeper in the valence/conduction bands. This effect suggests that n-type samples may have better thermoelectric performance with respect to p-type samples for which, the reduction of the concentration of Sn_{Bi} antisite defects appears as a necessary step to optimize their efficiency in the mid-temperature range.

Returning to the experimental results, the Hall coefficient R_H is positive for both samples in agreement with the sign of α, indicating holes as the dominant charge carriers. At 300 K, the Hall carrier concentration p_H is equal to 1.56±0.05×10^{20} cm^{-3} for $Sn_{0.99(1)}Bi_{2.00(1)}Te_{4.01(1)}$, which is slightly lower than that estimated from a Pisarenko plot in a prior study (2.2×10^{20} cm^{-3}).[36] For $Sn_{0.98(1)}Bi_{2.02(1)}Te_{3.99(1)}$, p_H is only slightly decreased to 1.11±0.03×10^{20} cm^{-3}, consistent with the higher ρ and α values with respect to the $Sn_{0.99(1)}Bi_{2.00(1)}Te_{4.01(1)}$ sample. According to the discussion above, we expect Sn_{Bi} antisite defects (contributing one hole per defect), to be the dominant defects in our samples. Small concentrations of Sn_{Bi} antisites of ~3.6 and 2.6% for $Sn_{0.99(1)}Bi_{2.00(1)}Te_{4.01(1)}$ and $Sn_{0.98(1)}Bi_{2.02(1)}Te_{3.99(1)}$, respectively, would explain the measured hole concentrations. The similar p_H values further indicate that the concentration of hole-like defects remains relatively similar from sample to sample, confirming that deviations from the ideal stoichiometry exist over a narrow compositional window at the annealing temperature considered herein (823 K). The situation is thus different from that of the parent compounds $Sn_{1-\delta}Te$ and Bi_2Te_3 for which the carrier concentration can vary by up to two orders of magnitude depending on the defect concentration.[1,72] p_H remains practically temperature-independent upon cooling to 5 K (Figure 11c), consistent with the highly-doped character of these samples. At 300 K, the values of the Hall mobility μ_H are similar for both samples, amounting to 38±2.7 cm^2 V^{-1} s^{-1} in the perpendicular direction (Figure 11d). Between 5 and ~100 K, μ_H remains constant to a value of ~75±5.2 cm^2 V^{-1} s^{-1} indicative of neutral impurity scattering. Above this temperature, μ_H decreases upon approaching 300 K following a temperature dependence close to $T^{-3/2}$, suggesting that acoustic phonon scattering becomes dominant around room temperature. Interestingly, the μ_H values remain similar in these two strongly-disordered samples and in the sample annealed for 75 days (see Figure S17 in SI). The lack of influence of the stacking disorder on the μ_H values might be due to the coherent interfaces between the different types of layers, thereby mitigating hole scattering. Of note, these values exceed those reported on single-crystalline $SnBi_2Te_4$ (Ref. 51) and are nearly three times higher than those reported in polycrystalline $SnSb_2Te_4$ (~13 cm^2 V^{-1} s^{-1} at 300 K) in the absence of stacking disorder.[60] In $SnBi_2Te_4$, these rather high mobility values may be afforded by the highly-dispersive valence bands giving rise to very low band effective masses, as predicted by our calculations.

The experimental α and p_H values measured at 300 K agree very well with the predicted Ioffe-Pisarenko curve. Within a single-parabolic band (SPB) model and assuming acoustic phonon scattering, these values correspond to a density-of-states effective mass m_{DOS}^* of $1.45m_e$, which also matches quite well our theoretical value of $m_{DOS}^* = 1.1m_e$ obtained by including Sn_{Bi} antisite defects.

Due to the contribution of the minority charge carriers to the transport above ~300 K, the power factor *PF* reaches its peak value of 1.0±0.1 mW m^{-1} K^{-1} at 330 K for both samples in the perpendicular direction due to the lower ρ values (Figure 14). Due to the concomitant increase in α and decrease in ρ values, higher *PF* values are obtained with respect to prior studies. However, this trend is reversed above 450 K, with the samples prepared in this study exhibiting lower *PF* values than in Ref. 36. This can be linked to the higher hole concentration achieved in this last study, which shifts the onset of the intrinsic regime towards higher temperatures.

As pertinent measures of the electronic quality of thermoelectric materials, the weighed mobility μ_w and thermoelectric quality factor B were calculated using the following relations

$$\mu_w = \mu_0 \left(\frac{m_{DOS}^*}{m_e}\right)^{3/2} \tag{3}$$

$$B = \left(\frac{k_B}{e}\right)^2 \frac{8\pi e\,(2m_0k_B)^{3/2}}{h^3} \frac{\mu_w T^{5/2}}{\kappa_{lat}} \tag{4}$$

where μ_0 is the intrinsic hole mobility calculated from the SPB model (~53±3.7 cm^2 V^{-1} s^{-1}), k_B is the Boltzmann constant, e is the elementary charge, h is Planck constant and κ_{lat} is the lattice thermal conductivity. The calculated μ_w value amounts to ~92±6.4 cm^2 V^{-1}s^{-1} for both samples. The value of the quality factor B of 0.11±0.02 at 300 K is lower than those reported for non-optimized Bi_2Te_3 samples (between 0.20 and 0.26) (Ref. 73) due to the lower κ_{lat} values achieved in $SnBi_2Te_4$ which do not counterbalance the decrease in mobility.

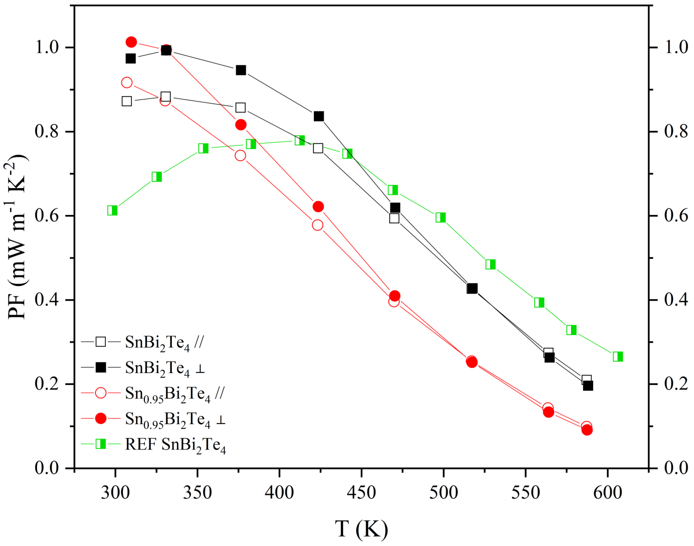

Figure 14. Temperature dependence of the power factor *PF* for $SnBi_2Te_4$ and $Sn_{0.95}Bi_2Te_4$ parallel and perpendicular to the pressing direction. For comparison, results reported in Ref. 36 have been added.

The temperature dependence of the total thermal conductivity κ is shown in Figure 15a. At 300 K, both samples have low κ values, ranging between 0.90±0.10 and 1.20±0.12 W m^{-1} K^{-1} along the parallel and perpendicular directions, respectively. Upon cooling, $\kappa(T)$ follows a temperature dependence typical of crystalline materials with a well-defined, low-temperature Umklapp peak centered at 30 K, with the magnitude of which varying between 1.60±0.08 and 2.10±0.10 W m^{-1} K^{-1}. The κ values measured along the parallel direction are lower than those measured perpendicularly due to the layered crystal structure of these compounds. The anisotropy in κ between these two directions is ~30%, and is reversed compared to the ρ values. In comparison to prior studies,[30,36,37] the present samples have higher κ values over the entire temperature range, consistent with the lower relative density of cold-pressed samples that lowers the κ values.

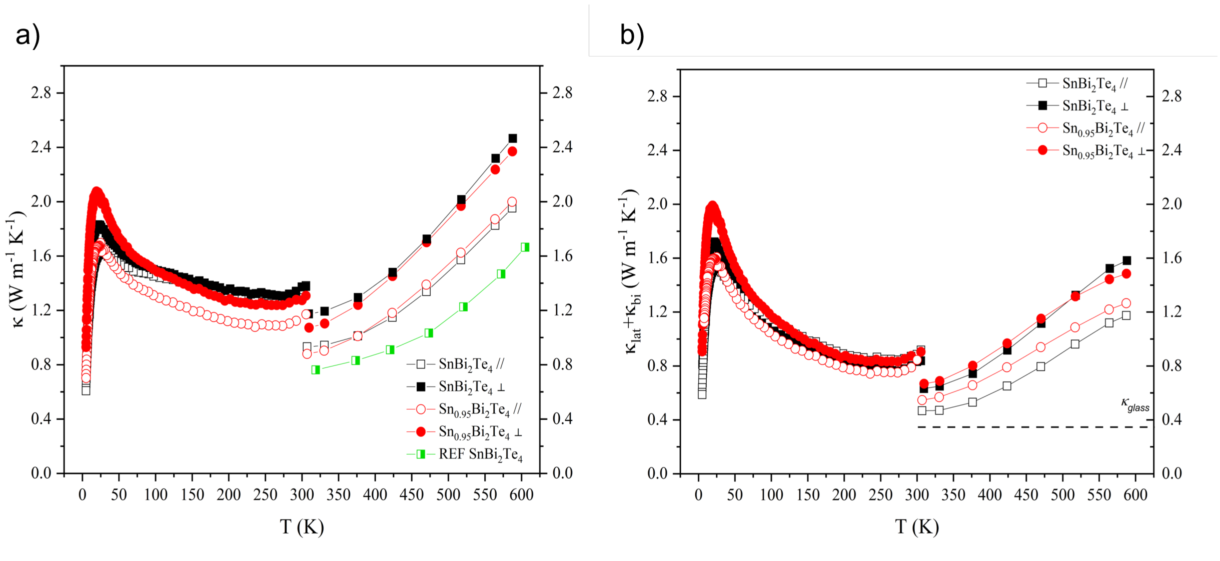

Figure 15. Temperature dependence of (a) the total thermal conductivity κ and (b) the sum of the lattice thermal conductivity κ_{lat} and bipolar contribution κ_{bi}. The mismatch in the κ values at 300 K is due to the contribution of thermal radiations that are inherent to the low-temperature measurement technique used. The horizontal dashed line stands for the glassy limit κ_{glass} of κ_{lat} according to the model of Cahill and Pohl.[74]

Above 300 K, κ increases with increasing temperature due to the contribution of thermally excited minority charge carriers that results in an additional bipolar contribution κ_{bi}. The lattice thermal conductivity κ_{lat} was calculated by subtracting the electronic contribution κ_{el} calculated using the Wiedemann–Franz law $\kappa_{el} = LT/\rho$, where L is the Lorenz number estimated by the SPB model. For both samples, κ_{lat} ranges between 0.50±0.06 to 0.70±0.09 W m^{-1} K^{-1} at 300 K in the parallel and perpendicular directions, respectively (Figure 15b). These values are close to the high-temperature glassy limit κ_{glass} of 0.30 W m^{-1} K^{-1}, inferred from the longitudinal and transverse sound velocities (v_L = 2860±85 m s^{-1} and v_T = 1782±53 m s^{-1}, respectively) measured at 300 K. These κ_{lat} values are similar to those achieved in other layered compounds of the family $(A^{IV}Te)_n(Bi_2X_3)_m$ such as in the substituted series $SnSb_2Te_{4-x}Se_x$, $Ge_{1-x}Sb_xBi_2Te_4$ or $PbBi_2Te_{4-x}Se_x$.[60,69,75]

In the sister compound $SnSb_2Te_4$,[76] lattice dynamics calculations have revealed high average Grüneisen parameters of the acoustic dispersions. Because the strength of phonon-phonon scattering is proportional to the square of this parameter, high values are usually observed in compounds with very low lattice thermal conductivity. Furthermore, these calculations, coupled with Raman spectroscopy, have evidenced the presence of low-frequency optical modes between 30 and 40 cm^{-1}, with the lowest Raman-active interlayer mode measured at 40 cm^{-1}. $SnBi_2Te_4$ might exhibit similar characteristics, in addition to a shift of the characteristic frequencies of the optical modes due to the mass contrast between Sb and Bi, which would further contribute to the low κ_{lat} values. This is consistent with the lower κ measured in $Sn_{0.99(1)}Bi_{2.00(1)}Te_{4.01(1)}$ (1.20±0.12 W m^{-1} K^{-1} at 300 K) with respect to $SnSb_2Te_4$ (2.10 W m^{-1} K^{-1} at 300 K).[36,60]

The favorable combination of very low lattice thermal conductivity and relatively high power factors results in peak *ZT* values of ~0.32±0.05 at 325 and 400 K for $Sn_{0.98(1)}Bi_{2.02(1)}Te_{3.99(1)}$ and $Sn_{0.99(1)}Bi_{2.00(1)}Te_{4.01(1)}$, respectively, in the parallel direction (Figure 16a). This peak *ZT* is similar to that measured in other pristine compounds of this family, such as in $SnSb_2Te_4$ or $GeBi_2Te_4$, and lower than those achieved upon forming solid solutions or doping,[60,69,75] with a maximum *ZT* of 0.55 achieved at 673 K in I-doped $SnSb_2Te_4$.[77]

The room-temperature hole concentrations in our two samples ($1.11\pm0.03\times10^{20}$ cm^{-3} and $1.56\pm0.05\times10^{20}$ cm^{-3}) are only slightly higher than the optimal value predicted by the SPB model (Figure 16b). Using the input parameters $m^*_{DOS} = 1.45m_e$, $\mu_0 = 53$ cm^2 V^{-1} s^{-1} and $\kappa_L = 0.65\pm0.08$ W m^{-1} K^{-1} (average value from the two samples in the perpendicular direction), the predicted optimum value is around 3×10^{19} cm^{-3} where a peak *ZT* of ~0.4 is achieved. Our two samples cluster around this optimum, indicating little room for further enhancing the thermoelectric performance at 300 K using donor-like impurities.

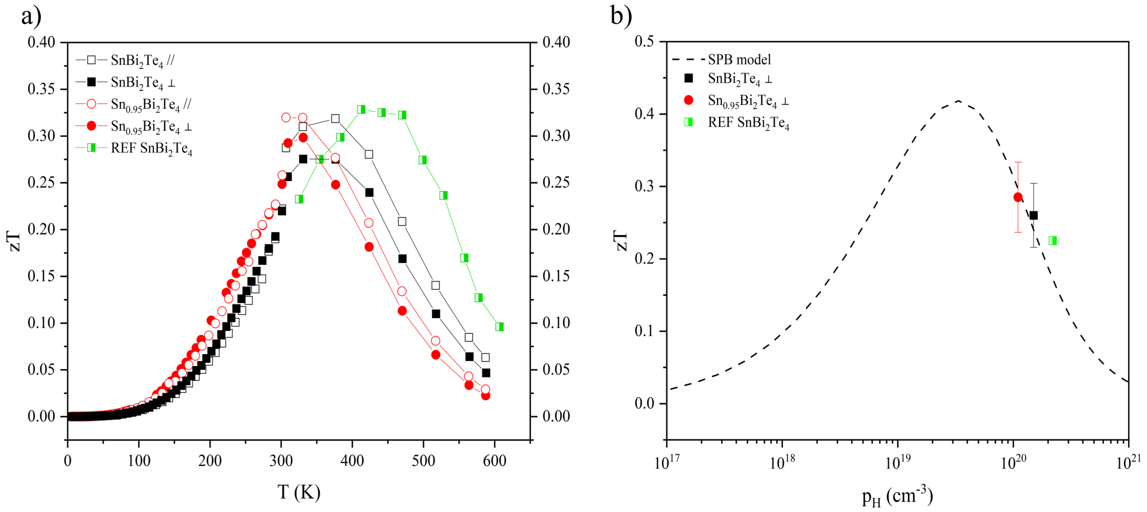

Figure 16. a) Temperature dependence of the dimensionless thermoelectric figure of merit *ZT*. b) Hole concentration dependence of *ZT* (solid curve) with the experimental values obtained herein and from Ref. 36.

Switching the majority carriers from holes to electrons may be a strategy worth pursuing due to the significant asymmetry between the conduction and valence band manifolds evidenced by our calculations. Recent theoretical considerations have shown that bipolar conduction effects can be mitigated in narrow-band-gap semiconductors exhibiting a large asymmetry parameter R_B.[19] This parameter is defined as $R_B = \mu_w^{maj}/\mu_w^{min}$, where μ_w^{maj} and μ_w^{min} are the weighed mobility of the majority (holes in the present case) and minority carriers expressed as $\mu_w = \frac{e\tau_0}{m_b^*} N_V \left(\frac{m_b^*}{m_e}\right)$ where m_b^* is the band effective mass, N_V the number of valleys and τ_0 is the relaxation time present in the energy dependence of the average relaxation time $\tau(E) \equiv \tau_0 \left(\frac{E}{k_B T}\right)^r$ with r being a parameter representing the scattering mechanism. Assuming as a first approximation that τ_0 is similar for holes and electrons, this ratio can be expressed as $\frac{\mu_w^{maj}}{\mu_w^{min}} \approx \frac{N_{V,v}}{N_{V,c}} \left(\frac{m_{b,v}^*}{m_{b,c}^*}\right)$ with N_v and N_c the number of valleys of the valence and conduction bands, respectively, and $m_{b,v}^*$ and $m_{b,c}^*$ the respective band effective mass. A R_B value higher than 1 corresponds to a strong asymmetry in favor of the majority carriers, thereby mitigating the detrimental influence of minority carriers. Using the values of these parameters inferred from our calculations ($N_v = 6$, $N_c = 2$, $m_{b,v}^* = 0.06m_e$ and $m_{b,c}^* = 0.31m_e$), $R_B \sim 0.6$ for $SnBi_2Te_4$. Thus, a strong asymmetry in m_b^* is observed but in favor of the minority carriers. This implies that better thermoelectric performance near room temperature may emerge in *n*-type samples for which $R_B \sim 1.7$, assuming that band parameters remain similar. This conclusion is in agreement with the calculated mobilities of holes and electrons (see Figure S16 in SI) showing that their ratio drops below 1.0 for *p*-type samples due to the presence of Sn_{Bi} antisite defects.

4. CONCLUSION

Polycrystalline samples of the layered chalcogenide $SnBi_2Te_4$ were synthesized by a combination of high-temperature melting reactions followed by annealing. Sn deficiency intentionally introduced in the sample $Sn_{0.98(1)}Bi_{2.02(1)}Te_{3.99(1)}$ leads to the presence of quintuple layers, suggesting the intergrowth of the $SnBi_4Te_7$ compound in agreement with the pseudo-binary SnTe–Bi_2Te_3 phase diagram. In agreement with measurements of the transport properties, *ab initio* calculations show that $SnBi_2Te_4$ is a *p*-type, narrow-band-gap semiconductor with a multivalley valence band structure. The bipolar conduction that sets in above room temperature is due to the presence of a few percent of Sn_{Bi} antisite defects, supported by ^{119}Sn Mössbauer spectroscopy, that modify the mobility ratio and shrink the band gap. The combination of low lattice thermal conductivity of the order of 0.50 W m^{-1} K^{-1} at 300 K and relatively high power factors leads to a peak *ZT* value of ~0.32±0.05 at 325 and 400 K for $Sn_{0.98(1)}Bi_{2.02(1)}Te_{3.99(1)}$ and $Sn_{0.99(1)}Bi_{2.00(1)}Te_{4.01(1)}$, respectively. Based on the SPB model, the hole concentrations are close to the optimum value predicted around 300 K, suggesting that alloying with non-rigid-band-like impurities might help to enhance the thermoelectric performance. Alternatively, investigating *n*-type samples may be an interesting strategy to pursue to take advantage of the large asymmetry between the valence and conduction bands, thereby possibly mitigating the detrimental influence of minority carrier effects. Finally, designing strategies aiming at decreasing the concentration of Sn_{Bi} antisite defects that limit the thermoelectric performance at high temperatures may be also considered in future studies.

ASSOCIATED CONTENT

Supporting Information

The Supporting Information is available free of charge at https://pubs.acs.org/doi/

Temperature dependence of the thermopower and electrical resistivity measured upon heating and cooling; Sketch of the Brillouin zone with the high-symmetry points; Orbital decomposition of the DOS of $SnBi_2Te_4$; Calculated power factor PF as a function of carrier concentration at T = 100, 300 and 700 K; Fits of the experimental Mössbauer spectrum; Dependence of the fitted quadrupole splitting QS(p) of the doublet; Additional discussion of the Mössbauer analysis; PXRD patterns of $Sn_{0.98(1)}Bi_{2.02(1)}Te_{3.99(1)}$ and $Sn_{0.99(1)}Bi_{2.00(1)}Te_{4.01(1)}$ collected before and after annealing for 10 days; Rietveld refinements of the PXRD patterns of $Sn_{0.98(1)}Bi_{2.02(1)}Te_{3.99(1)}$ and $Sn_{0.99(1)}Bi_{2.00(1)}Te_{4.01(1)}$ annealed for 10 days and of $SnBi_2Te_4$ annealed for 75 days; PXRD patterns collected on bulk pieces cut parallel and perpendicular to the pressing direction; SEM images in backscattered electron (BSE) mode and corresponding elemental X-ray maps for $Sn_{0.98(1)}Bi_{2.02(1)}Te_{3.99(1)}$ and $Sn_{0.99(1)}Bi_{2.00(1)}Te_{4.01(1)}$ annealed for 10 days; Additional discussion and HAADF-STEM images taken on the $Sn_{0.99(1)}Bi_{2.00(1)}Te_{4.01(1)}$ and $Sn_{0.98(1)}Bi_{2.02(1)}Te_{3.99(1)}$ samples annealed for 10 days; Comparison of the transport properties of $SnBi_2Te_4$ samples annealed for 10 and 75 days; Energy dependent mobility ratio for electrons and holes in $SnBi_2Te_4$; Additional calculations of the temperature dependence of the thermopower and electronic density of states with Bi_{Sn} antisite defects; Calculations of the DOS of $SnBi_2Te_4$ with a small concentration of Sn vacancies.

AUTHOR INFORMATION

Corresponding Authors

Christophe Candolfi - *Institut Jean Lamour, UMR 7198 CNRS – Université de Lorraine, 2 allée André Guinier-Campus ARTEM, BP 50840, 54011 Nancy Cedex, France*

orcid.org/0000-0002-1248-5354; Email: christophe.candolfi@univ-lorraine.fr

Bartlomiej Wiendlocha - *AGH University of Krakow, Faculty of Physics and Applied Computer Science, Aleja Mickiewicza 30, 30-059 Krakow, Poland*

orcid.org/ 0000-0001-9536-7216; Email: wiendlocha@fis.agh.edu.pl

Authors

Ilayda Terzi - *Institut Jean Lamour, UMR 7198 CNRS – Université de Lorraine, 2 allée André Guinier-Campus ARTEM, BP 50840, 54011 Nancy Cedex, France* ; orcid.org/0009-0000-3544-956X

Kacper Pryga - *AGH University of Krakow, Faculty of Physics and Applied Computer Science, Aleja Mickiewicza 30, 30-059 Krakow, Poland*; orcid.org/0000-0003-3087-7498

Petr Levinský - *FZU – Institute of Physics of the Czech Academy of Sciences, Cukrovarnická 10/112, 162 00, Prague 6, Czech Republic*; orcid.org/0000-0002-8501-1256

Soufiane El Oualid - *Institut Jean Lamour, UMR 7198 CNRS – Université de Lorraine, 2 allée André Guinier-Campus ARTEM, BP 50840, 54011 Nancy Cedex, France* ; orcid.org/0000-0001-9634-8754

Sylvie Migot - *Institut Jean Lamour, UMR 7198 CNRS – Université de Lorraine, 2 allée André Guinier-Campus ARTEM, BP 50840, 54011 Nancy Cedex, France* ; orcid.org/0000-0003-3803-9931

Jaafar Ghanbaja - *Institut Jean Lamour, UMR 7198 CNRS – Université de Lorraine, 2 allée André Guinier-Campus ARTEM, BP 50840, 54011 Nancy Cedex, France* ; orcid.org/0000-0003-2870-0570

Christine Gendarme - *Institut Jean Lamour, UMR 7198 CNRS – Université de Lorraine, 2 allée André Guinier-Campus ARTEM, BP 50840, 54011 Nancy Cedex, France* ; orcid.org/0000-0002-1193-4453

Thierry Schweitzer - *Institut Jean Lamour, UMR 7198 CNRS – Université de Lorraine, 2 allée André Guinier-Campus ARTEM, BP 50840, 54011 Nancy Cedex, France*

Bernard Malaman - *Institut Jean Lamour, UMR 7198 CNRS – Université de Lorraine, 2 allée André Guinier-Campus ARTEM, BP 50840, 54011 Nancy Cedex, France* ; orcid.org/0000-0001-8989-6955

Gérard Le Caër - *Institut de Physique de Rennes, UMR UR1-CNRS 6251, Université de Rennes I, Campus de Beaulieu, 35042 Rennes Cedex, France* ; orcid.org/0000-0001-5316-7996

Bertrand Lenoir - *Institut Jean Lamour, UMR 7198 CNRS – Université de Lorraine, 2 allée André Guinier-Campus ARTEM, BP 50840, 54011 Nancy Cedex, France* ; orcid.org/0000-0001-9631-4925

Author contribution

I. T. and K. P. have equally contributed to this work.

Notes

The authors declare no competing financial interest.

ACKNOWLEDGMENTS

I.T., C.C. and B.L. acknowledge the financial support from the French National Agency (ANR) in the frame of the project HYDRES (project identifier ANR-21-CE50-0003).

REFERENCES

(1) Rowe, D. M. Ed., *Thermoelectrics and its Energy Harvesting,* Boca Raton: CRC Press, 2012.

(2) Yan, Q.; Kanatzidis, M. G. High-performance thermoelectrics and challenges for practical devices. *Nat. Mater.* 2022, *21*, 503–513.

(3) Goldsmid, H. J. *Thermoelectric Refrigeration*; Springer: New York, 1964.

(4) Heremans, J. P.; Jovovic, V.; Toberer, E. S.; Saramat, A.; Kurosaki, K.; Charoenphakdee, A.; Yamanaka, S.; Snyder, G. J. Enhancement of Thermoelectric Efficiency in PbTe by Distortion of the Electronic Density of States. *Science* **2008**, *321*, 554–557.

(5) Heremans, J. P.; Wiendlocha, B.; Chamoire, A. M. Resonant Levels in Bulk Thermoelectric Semiconductors. *Energy Environ. Sci.* **2012**, *5*, 5510–5530.

(6) Wiendlocha, B.; Misra, S.; Dauscher, A.; Lenoir, B.; Candolfi, C. Residual Resistivity as an Independent Indicator of Resonant Levels in Semiconductors. *Mater. Horiz.* **2021**, *8*, 1735–1743.

(7) Pei, Y.; Shi, X.; LaLonde, A.; Wang, H.; Chen L.; Snyder, G. J. Convergence of Electronic Bands for High Performance Bulk Thermoelectrics. *Nature* **2011**, *473*, 66–69.

(8) Zhang, J.; Liu, R.; Cheng, N.; Zhang, Y.; Yang, J.; Uher, C.; Shi, X.; Chen L.; Zhang, W. High-performance Pseudocubic Thermoelectric Materials from Non-Cubic Chalcopyrite Compounds. *Adv. Mater.* **2014**, *26*, 3848–3853.

(9) Dong, Y.; Khabibullin, A. R.; Wei, K.; Salvador, J. R.; Nolas, G. S.; Woods, L. M. Bournonite $PbCuSbS_3$: Stereochemically Active Lone-Pair Electrons that Induce Low Thermal Conductivity. *Chem. Phys. Chem.* **2015**, *16*, 3264–3270.

(10) Zheng, Y.; Slade, T. J.; Hu, L.; Tan, X. Y.; Luo, Y.; Luo, Z.-Z.; Xu, J.; Yan, Q.; Kanatzidis, M. G. Defect engineering in thermoelectric materials: what have we learned? *Chem. Soc. Rev.* **2021**, *50*, 9022–9054.

(11) Lu, X.; Morelli, D. T.; Xia, Y.; Zhou, F.; Ozolins, V.; Chi, H.; Zhou, X.; Uher, C. High Performance Thermoelectricity in Earth-Abundant Compounds Based on Natural Mineral Tetrahedrites. *Adv. Energy Mater.* **2012**, *3*, 342–348.

(12) Li, C. W.; Hong, J.; May, A. F.; Bansal, D.; Chi, S.; Hong, T.; Ehlers, G.; Delaire, O. Orbitally driven giant phonon anharmonicity in SnSe. *Nat. Phys.* **2015**, *11*, 1063–1069.

(13) Jood, P.; Ohta, M.; Yamamoto, A.; Kanatzidis, M. G. Excessively Doped PbTe with Ge-Induced Nanostructures Enables High-Efficiency Thermoelectric Modules. *Joule* **2018**, *2*, 1339–1355.

(14) Mao, J.; Chen, G.; Ren, Z. Thermoelectric cooling materials. *Nat. Mater.* **2021**, *20*, 454–461.

(15) Lee, H.; Kim, T.; Son, S. C.; Kim, J.; Kim, D.; Lee, J.; Chung, I. Unique Microstructures and High Thermoelectric Performance in *n*-type $Bi_2Te_{2.7}Se_{0.3}$ by the Dual Incorporation of Cu and Y. *Mater. Today Phys.* **2023**, *31*, 100986.

(16) Zhu, B.; Liu, X.; Wang, Q.; Shu, Z.; Guo, Z.; Tong, Y.; Cui, J.; Gu, M.; He, J. Realizing record high performance in *n*-type Bi_2Te_3-based thermoelectric materials. *Energy Environ. Sci.* **2020**, *13*, 2106–2114.

(17) Deng, R.; Su, X.; Zheng, Z.; Liu, W.; Yan, Y.; Zhang, Q.; Dravid, V. P.; Uher, C.; Kanatzidis, M. G. Thermal conductivity in $Bi_{0.5}Sb_{1.5}Te_{3+x}$ and the role of dense dislocation arrays at grain boundaries. *Sci. Adv.* **2018**, *4*, eaar5606.

(18) Mao, J.; Zhu, H.; Ding, Z.; Liu, Z.; Gamage, G. A.; Chen, G.; Ren, Z. High thermoelectric cooling performance of *n*-type Mg_3Bi_2-based materials. *Science* **2019**, *365*, 495–498.

(19) Imasato, K.; Wood, M.; Anand, S.; Kuo, J. J.; Snyder, G. J. Understanding the High Thermoelectric Performance of Mg_3Sb_2-Mg_3Bi_2 Alloys. *Adv. Energy Sustainability Res.* **2022**, *3*, 2100208.

(20) Lenoir, B.; Dauscher, A.; Cassart, M.; Ravich, Yu. I.; Scherrer, H. Effect of antimony content on the thermoelectric figure of merit of $Bi_{1-x}Sb_x$ alloys. *J. Phys. Chem. Solids* **1998**, *59*, 129–134.

(21) Chung, D.-Y.; Hogan, T.; Brazis, P.; Rocci-Lane, M.; Kannewurf, C.; Bastea, M.; Uher, C.; Kanatzidis, M. $CsBi_4Te_6$: A High-Performance Thermoelectric Material for Low-Temperature Applications. *Science* **2000**, *287*, 1024–1027.

(22) Toriyama, M. Y.; Carranco, A. N.; Snyder, G. J.; Gorai, P. Material descriptors for thermoelectric performance of narrow-gap semiconductors and semimetals. *Mater. Horiz.* **2023**, *10*, 4256–4269.

(23) Vilaplana, R.; Sans, J. A.; Manjon, F. J.; Andrada-Chacon, A.; Sanchez-Benitez, J.; Popescu, C.; Gomis, O.; Pereira, A. L. J.; Garcia-Domene, B.; Rodriguez-Hernandez, *et al.* Structural and electrical study of the topological insulator $SnBi_2Te_4$ at high pressure. *J. Alloys Compd.* **2016**, *685*, 962–970.

(24) Pal, S.; Arora, R.; Banik, A.; Glazyrin, K. V.; Muthu, D. V. S.; Biswas, K.; Waghmare, U. V.; Sood, A. K. Pressure-induced topological and structural phase transitions in natural van der Waals heterostructures from the $(SnTe)_m(Bi_2Te_3)_n$ homologous family: Raman spectroscopy, X-ray diffraction, and density functional theory. *Phys. Rev. B* **2022**, *106*, 134104.

(25) Eremeev, S. V.; Landolt, G.; Menshchikova, T. V.; Slomski, B.; Koroteev, Y. M.; Aliev, Z. S.; Babanly, M. B.; Henk, J.; Ernst, A.; Patthey, L.; *et al.* Atom-specific spin mapping and

buried topological states in a homologous series of topological insulators. *Nat. Commun.* **2012**, *3*, 635.

(26) Li, J.; Li, Y.; Du, S.; Wang, Z.; Gu, B.-L.; Zhang, S.-C.; He, K.; Duan, W.; Xu, Y. Intrinsic magnetic topological insulators in van der Waals layered $MnBi_2Te_4$-family materials. *Sci. Adv.* **2019**, *5*, eaaw5685.

(27) Deng, Y.; Yu, Y.; Shi, M. Z.; Guo, Z.; Xu, Z.; Wang, J.; Chen, X. H.; Zhang, Y. Quantum anomalous Hall effect in intrinsic magnetic topological insulator $MnBi_2Te_4$. *Science* **2020**, *367*, 895–900.

(28) McGuire, M. A.; Zhang, H.; May, A. F.; Okamoto, S.; Moore, R. G.; Wang, X.; Girod, C.; Thomas, S. M.; Ronning, F.; Yan, J. Superconductivity by alloying the topological insulator $SnBi_2Te_4$. *Phys. Rev. Mater.* **2023**, *7*, 034802.

(29) Shelimova, L. E.; Karpinskii, O. G.; Konstantinov, P. P.; Avilov, E. S.; Kretova, M. A.; Zemskov, V. S. Crystal Structures and Thermoelectric Properties of Layered Compounds in the ATe–Bi_2Te_3 (A = Ge, Sn, Pb) Systems. *Inorg. Mater.* **2004**, *40*, 451–460.

(30) Pan, L.; Li, J.; Bérardan, D.; Dragoe, N. Transport properties of the $SnBi_2Te_4$–$PbBi_2Te_4$ solid solution. *J. Solid State Chem.* **2015**, *225*, 168–173.

(31) Tak, J.-Y.; Lim, Y. S.; Kim, J. N.; Lee, C.; Shim, J. H.; Cho, H. K.; Park, C.-H.; Seo, W.-S. Thermoelectric transport properties of tetradymite-type $Pb_{1-x}Sn_xBi_2Te_4$ compounds. *J. Alloys Compd.* **2017**, *690*, 966–970.

(32) Karpinskii, O. G.; Shelimova, L. E.; Kretova, M. A.; Avilov, E. S.; Zemskov, V. S. X-ray Diffraction Study of Mixed-Layer Compounds in the Pseudobinary System SnTe–Bi_2Te_3. *Inorg. Mater.* **2003**, *39*, 240–246.

(33) Reynolds, R. A. Phase Relations and Thermoelectric Properties of the Alloy Systems SnTe-Bi_2Te_3 and PbTe-Sb_2Te_3. *J. Electrochem. Soc.* **1967**, *114*, 526–530.

(34) Chiu, C.; Hsu, C.; Chen, S.; Wu, H. Phase Equilibria of the Sn-Bi-Te Ternary System. *J. Electron. Mater.* **2012**, *41*, 22–31.

(35) Adouby, K; Touré, A. A.; Kra, G.; Olivier-Fourcade, J.; Jumas, J.-C.; Perez Vicente, C. Phase diagram and local environment of Sn and Te: SnTe-Bi and SnTe-Bi_2Te_3 systems. *Comptes Rendus Académie Sci. - Ser. IIC - Chem.* **2000**, *3*, 51–58.

(36) Kuropatwa, B. A.; Kleinke, H. Thermoelectric Properties of Stoichiometric Compounds in the $(SnTe)_x(Bi_2Te_3)_y$ System. *Z. Für Anorg. Allg. Chem.* **2012**, *638*, 2640–2647.

(37) Kuropatwa, B. A.; Assoud, A.; Kleinke, H. Effects of Cation Site Substitutions on the Thermoelectric Performance of Layered $SnBi_2Te_4$ utilizing the Triel Elements Ga, In, and Tl: Cation Site Substitutions of Layered $SnBi_2Te_4$ with Ga, In, and Tl. *Z. Für Anorg. Allg. Chem.* **2013**, *639*, 2411–2420.

(38) Rodriguez-Carvajal, J. Fullprof Program. *Physica B* **1993**, *192*, 55–69.

(39) Alleno, E.; Bérardan, D.; Byl, C.; Candolfi, C.; Daou, R.; Decourt, R.; Guilmeau, E.; Hébert, S.; Hejtmanek, J.; Lenoir, B.; *et al.* A round robin test of the uncertainty on the measurement of the thermoelectric dimensionless figure of merit of $Co_{0.97}Ni_{0.03}Sb_3$. *Rev. Sci. Instrum.* **2015**, *86*, 011301.

(40) Kresse, G.; Hafner, J. Ab initio molecular dynamics for liquid metals. *Phys. Rev. B* **1993**, *47*, 558–561.

(41) Kresse, G.; Hafner, J. Ab initio molecular-dynamics simulation of the liquid-metal–amorphous-semiconductor transition in germanium. *Phys. Rev. B* **1994**, *49*, 14251–14269.

(42) Kresse, G.; Furthmüller, J. Efficiency of ab-initio total energy calculations for metals and semiconductors using a plane-wave basis set. *Comput. Mater. Sci.* **1996**, *6*, 15–50.

(43) Kresse, G.; Furthmüller, J. Efficient iterative schemes for ab initio total-energy calculations using a plane-wave basis set. *J. Phys. Rev. B* **1996**, *54*, 11169–11186.

(44) Kresse, G.; Joubert, D. From Ultrasoft Pseudopotentials to the Projector Augmented-Wave Method. *Phys. Rev. B* **1999**, *59*, 1758–1775.

(45) Blöchl, P. E. Projector augmented-wave method. *Phys. Rev. B* **1994**, *50*, 17953–17979.

(46) Ceperley, D. M.; Alder, B. J. Ground State of the Electron Gas by a Stochastic Method. *Phys. Rev. Lett.* **1980**, *45*, 566–569.

(47) Perdew, J. P.; Zunger, A. Self-interaction correction to density-functional approximations for many-electron systems. *Phys. Rev. B* **1981**, *23*, 5048–5079.

(48) Blaha, P.; Schwarz, K.; Tran, F.; Laskowski, R. Madsen, G. K. H.; Marks, L. D. WIEN2k: An APW+lo program for calculating the properties of solids. *J. Chem. Phys.* **2020**, *152*, 074101.

(49) Tran, F.; Blaha, P. Accurate Band Gaps of Semiconductors and Insulators with a Semilocal Exchange-Correlation Potential. *Phys. Rev. Lett.* **2009**, *102*, 226401.

(50) Madsen, G. K. H.; Singh, D. J. BoltzTraP. A code for calculating band-structure dependent quantities. *Comput. Phys. Commun.* **2006**, *175*, 67–71.

(51) Saxena, A.; Navneet, N. K.; Sharma, M. M.; Awana, V. P. S. Detailed structural and topological analysis of $SnBi_2Te_4$ single crystal. *J. Phys. Chem. Solids* **2023**, *174*, 111169.

(52) Heremans, J. P.; Wiendlocha, B. Tetradymites: Bi_2Te_3-Related Materials, in *Materials Aspect of Thermoelectricity*, Ed. C. Uher, CRC Press, 2016.

(53) Eremeev, S. V.; De Luca, O.; Sheverdyaeva, P. M.; Ferrari, L.; Matetskiy, A. V.; Di Santo, G.; Petaccia, L.; Crovara, C.; Caruso, T.; Papagno, M.; *et al.* Energy-overlap of the Dirac surface state with bulk bands in $SnBi_2Te_4$. *Phys. Rev. Mater.* **2023**, *7*, 014203.

(54) Kutorasinski, K.; Wiendlocha, B.; Tobola, J.; Kaprzyk, S. Importance of relativistic effects in electronic structure and thermopower calculations for Mg_2Si, Mg_2Ge, and Mg_2Sn. *Phys. Rev. B* **2014**, *89*, 115205.

(55) Menshchikova, T. V.; Eremeev, S. V.; Koroteev, Yu. M.; Kuznetsov, V. M., Chulkov, E. V. Ternary compounds based on binary topological insulators as an efficient way for modifying the Dirac cone. *JETP Lett.* **2011**, *93*, 15–20.

(56) Dalui, T. K.; Das, B.; Barman, C. K.; Ghose, P. K.; Sarma, A.; Mahatha, S. K.; Diekmann, F.; Rossnagel, K.; Majumdar, S.; Alam, A.; *et al*. Unconventional electronic phase transition in $SnBi_2Te_4$. *J. Phys.: Condens. Matter* **2023**, *35*, 465701.

(57) Zou, Y.-C.; Chen, Z.-G.; Zhang, E.; Kong, F.; Lu, Y.; Wang, L.; Drennan, J.; Wang, Z.; Xiu, F.; Cho, K.; *et al*. Atomic disorders in layer structured topological insulator $SnBi_2Te_4$ nanoplates. *Nano Res.* **2017**, *11*, 696–706.

(58) Fragkos, S.; Baringthon, L.; Tsipas, P.; Xenogiannopoulou, E.; Le Fèvre, P.; Kumar, P.; Okuno, H.; Reyren, N.; Lemaitre, A.; Patriarche, G.; *et al*. A. Topological surface states in epitaxial $(SnBi_2Te_4)_n(Bi_2Te_3)_m$ natural van der Waals superlattices. *Phys. Rev. Mater.* **2021**, *5*, 014203.

(59) Kutorasinski, K.; Wiendlocha, B.; Kaprzyk, S.; Tobola, J. Electronic structure and thermoelectric properties of *n*- and *p*-type SnSe from first-principles calculations. *Phys. Rev. B* **2015**, *91*, 205201.

(60) Wu, H.; Lu, X.; Wang, G.; Peng, K.; Zhang, B.; Chen, Y.; Gong, X.; Tang, X.; Zhang, X.; Feng, Z.; *et al*. Strong lattice anharmonicity securing intrinsically low lattice thermal conductivity and high performance thermoelectric $SnSb_2Te_4$ via Se alloying. *Nano Energy* **2020**, *76*, 105084.

(61) Kuznetsova, L. A.; Kuznetsov, V.L.; Row, D.M. Thermoelectric properties and crystal structure of ternary compounds in the Ge(Sn,Pb)Te–Bi_2Te_3 systems. *J. Phys. Chem. Solids.* **2000**, *61*, 1269–1274.

(62) Ledda, F.; Muntoni, C.; Serci, S.; Pellerito, L. Ordering of metal atoms in the SnTe-Bi_2Te_3 system. *Chem. Phys. Lett.* **1987**, *134*, 545–548.

(63) Oeckler, O.; Schneider, M. N.; Fahrnbauer, F.; Vaughan, G. Atom distribution in $SnSb_2Te_4$ by resonant X-ray diffraction. *Solid State Sci.* **2011**, *13*, 1157–1161.

(64) Hightower, A.; Delcroix, P.; Le Caër, G.; Huang, C.-K.; Ratnakumar, B. V.; Ahn, C. C.; Fultz, B. A ^{119}Sn Mössbauer Spectrometry Study of Li-SnO Anode Materials for Li-Ion Cells. *J. Electrochem. Soc.* **2000**, *147*, 1–8.

(65) Soulmi, N.; D. Dambournet, D.; Rizzi, C.; Sirieix-Plenet, J.; Duttine, M.; Wattiaux, A.; Swiatowska, J.; Borkiewicz, O.J.; Groult, H.; Gaillon, L. Structural and Morphological Description of Sn/SnO_x Core−Shell Nanoparticles Synthesized and Isolated from Ionic Liquid. *Inorg. Chem.* **2017**, *56*, 10099−10106.

(66) Nentwig, M.; Eisenburger, L.; Heinke, F.; Souchay, D.; Oeckler, O. A layered tin bismuth selenide with three different building blocks that account for an extremely large lattice parameter of 283 Å. *Chem. Euro. J.* **2020**, *26*, 10676–10681.

(67) Bos, J. W. G.; Zandbergen, H. W.; Lee, M.-H.; Ong, N. P.; Cava, R. J. Structures and thermoelectric properties of the infinitely adaptive series $(Bi_2)_m(Bi_2Te_3)_n$. *Phys. Rev. B* **2007**, *75*, 195203.

(68) Frangis, N.; Kuypers, S.; Manolikas, C.; Van Landuyt, J.; Amelinckx, S. Continuous series of one-dimensional structures in the compounds $Bi_{2+x}Se_3$, $Bi_{2+x}Te_3$, $Sb_{2+x}Te_3$, $(Bi_2Te_3)_n$GeTe and $(Sb_2Te_3)_n$GeTe. *Solid State Commun.* **1989**, *69*, 817–819.

(69) Dong, J.; Hu, L.; Liu, J.; Liu, Y.; Jiang, Y.; Yu, Z.; Tan, X. Y.; Suwardi, A.; Zheng, Q.; Li, Q.; *et al.* Off-Centering of Ge Atoms in $GeBi_2Te_4$ and Impact on Thermoelectric Performance. *Adv. Funct. Mater.* **2024**, 2314499.

(70) Goldsmid, H. J.; Sharp, J. W. Estimation of the thermal band gap of a semiconductor from seebeck measurements. *J. Electron. Mater.* **1999**, *28*, 869–872.

(71) Gibbs, Z. M.; Kim, H.-S.; Wang, H.; Snyder, G. J. Band gap estimation from temperature dependent Seebeck measurement—Deviations from the $2e|S|_{max}T_{max}$ relation. *Appl. Phys. Lett.* **2015**, *106*, 022112.

(72) Ibrahim, D.; Candolfi, C.; Migot, S.; Ghanbaja, J.; Dauscher, A.; Le Caër, G.; Malaman, B.; Semprimoschnig, C.; Lenoir, B. Comprehensive study of the low-temperature transport properties of polycrystalline $Sn_{1+x}Te$ ($x = 0$ and 0.03). *Phys. Rev. Mater.* **2019**, *3*, 085404.

(73) Witting, I. T.; Chasapis, T. C.; Ricci, F.; Peters, M.; Heinz, N. A.; Hautier, G.; Snyder, G. J. The Thermoelectric Properties of Bismuth Telluride. *Adv. Electron. Mater.* **2019**, *5*, 1800904.

(74) Cahill, D. G.; Watson, S. K.; Pohl, R. O. Lower limit to the thermal conductivity of disordered crystals. *Phys. Rev. B* **1992**, *46*, 6131–6140.

(75) Qian, X.; Jin, H.; Li, X.; Ding, B.; Wang, J.; Wang, S.-F. Enhanced thermoelectric properties of layered anisotropic $PbBi_2Te_4$ through the suppression of bipolar diffusion effect via Se alloying. *Appl. Phys. Lett.* **2024**, *124*, 103902.

(76) Sans, J. A.; Vilaplana, R.; Lora da Silva, E.; Popescu, C.; Cuenca-Gotor, P.; Andrada-Chacon, A.; Sanchez-Benitez, J.; Gomis, O.; Pereira, A. L. J.; Rodriguez-Hernandez, P.; *et al.* Characterization and Decomposition of the Natural van der Waals $SnSb_2Te_4$ under Compression. *Inorg. Chem.* **2020**, *59*, 9900–9918.

(77) Das, S.; Sarkar, D.; Biswas, K. Enhanced Topological Surface State Mediated Transport Elevates Thermoelectric Performance in $SnSb_2Te_4$ Quantum Material. *Chem. Mater.* **2024**, 36, 3359–3368.

TOC Graphic